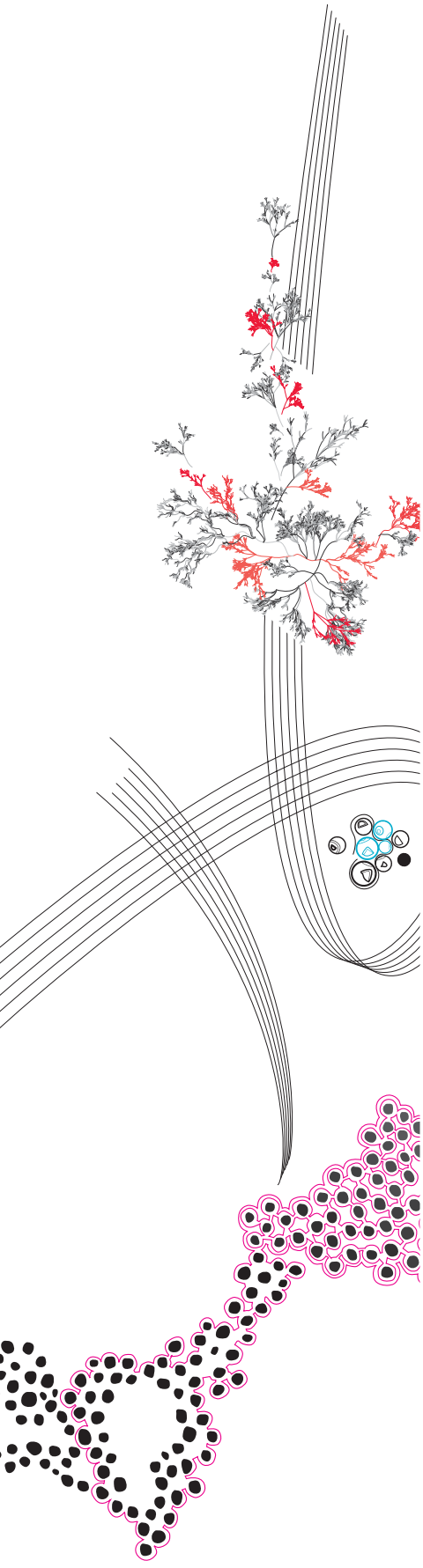

MSc Thesis Mechanical Engineering

Design of a Flexible Hinge for an Atmospheric Dispersion Corrector

W.E. Kamphof

Chairman:	Prof.dr.ir. D.M Brouwer
Supervisors:	Dr.ir. M. Nijenhuis
	Ing. J.W. Kragt
	Dr. M.A. Lewińska-Maresca

October 27, 2023

Faculty of Engineering Technology
Chair of Precision Engineering

UNIVERSITY OF TWENTE.

Preface

The thesis you are about to read is the result of my MSc assignment 'Design of a Flexible Hinge for an Atmospheric Dispersion Corrector', the culmination of my academic endeavors at the University of Twente. The research and writing process took place from December 2022 until October 2023, and represents my fulfillment of the graduation requirements.

Ever since the beginning of my academic journey, I have been interested in the 'grey area' between physics and mechanical engineering. The provided research opportunity was pursued to challenge myself to conduct research in this area, delving into the intricate world of astronomy and discovering relations between mechanical designs and astronomical observations.

First of all, I want to express my appreciation to my daily supervisor, Marijn Nijenhuis, for his guidance and contributions throughout the process. The insights you have given during our many meetings have refined the contents of this thesis, and the advice concerning the software was essential for the result.

Secondly, I want to thank the chairman, Dannis Brouwer, and my other supervisors, Jan Kragt, and Mirka Maresca, for their support and guidance during this thesis.

Lastly, I would like to thank everyone at Astron Nova, where this research has been carried out. The kind and motivated colleagues and the great ambiance at the company have certainly left an impression. I hope our collaboration will not be terminated with the completion of this thesis.

Wilbert Kamphof
't Harde, Oktober 2023

Abstract

Compliant mechanisms often have the advantage of high precision at the cost of a limited range of motion. In this research, a hollow compliant hinge is developed for use in an Atmospheric Dispersion Corrector (ADC) commonly found in large telescopes. This device contains two sets of optical prisms to correct for the unwanted dispersion effect that occurs when light meets the atmosphere under an angle. These prisms must perform a near-pure rotation around the optical axis, which must not be obstructed by the geometry of the ADC. This study strives to achieve the required deflection range of a single Degree of Freedom design while having sufficiently high unwanted eigenfrequencies, support stiffness, and low stress levels. Many concepts were developed using the software *SPACAR Light*, of which two could be optimized to meet the requirements of the ADC. Furthermore, the final concepts were modeled in the software *SolidWorks* and simulated in the Finite Element Method software *Ansys*.

The research showed that a large stroke in combination with low stress levels and high support stiffness is possible through radially symmetric compounded designs. However, a compounded design is underconstrained and has low associated unwanted eigenfrequencies. Both high kinematic- and dynamic performance is achieved through the addition of a kinematic coupler, or synchronizer. A design called the *Compounded Torsion Pivot* (CTP) is explored with the addition of such a synchronizer. The monolithic design called the *Large Angle Flexure Pivot* (LAFP) is also analyzed and expanded with a synchronizer. While both designs meet the requirements for the ADC, the LAFP ultimately outperforms the CTP with better kinematic- and dynamic characteristics. Furthermore, the LAFP is easier to produce using a combination of Wire EDM and milling.

Contents

1 Introduction

Astronomers often depend on the very best observatories for their scientific discoveries. With a primary mirror of almost 40 meters, the Extremely Large Telescope (ELT) is the largest optical/near-infrared telescope under construction, expected to assist in major advancements in the fields of Physics and Astronomy. The telescope will be used for research in the solar system, exoplanets, stars, black holes, galaxies, fundamental physics, cosmology, and dark matter. Because the telescope will not be carried into the vacuum of space but will be built in the desert of Chile, light rays must travel through the atmosphere to the primary mirror. Therefore, the effects caused by atmospheric distortion must be corrected while observing.

One of the instruments on the ELT is the Multi-AO Imaging Camera for Deep Observations (or MICADO). The near-infrared nature makes the instrument ideal for identifying exoplanets, but also for resolving individual stars in the other galaxies and investigating the center of the milky way. The instrument is placed within a cryostat, which is essential for near-infrared detectors. The observed infrared beam passes into the cryostat, after which it is collimated, filtered depending on the astronomical observation, and passed through the Atmospheric Dispersion Corrector (ADC) and one of four exchangeable sets of optical components.

The ADC is responsible for the correction of dispersion caused by different refraction angles when light enters the atmosphere. One can imagine the atmosphere as a prism, causing the observed object to appear blurred and stretched into different colors (figure 1). The ADC corrects for this effect using two sets of prisms, which are rotated such that the light is refracted back to a single focal point on the detector. At the time of writing, the design of the ADC in MICADO barely meets the accuracy requirements to counter the dispersion effects and suffers from significant wear on friction wheels that rotate the prisms in the cryostat. To future-proof these issues, this work concerns an alternative design of the ADC using a flexure mechanism for precision guiding the prism set.

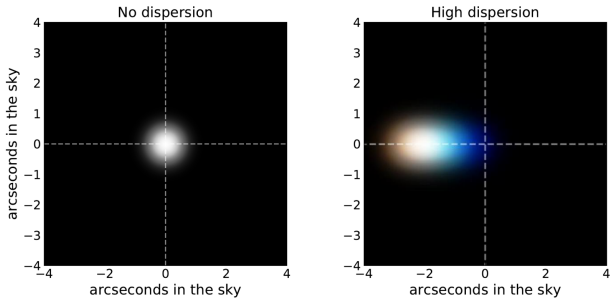

Fig. 1 Effects of atmospheric dispersion with a zenith angle of 0° (left) and 60° (right).[36]

Atmospheric Dispersion Correction

A fundamental understanding of the atmospheric dispersion effect is essential for the development of a redesign. Atmospheric dispersion is the difference in the angle of refraction between two light rays with different wavelengths after they pass through the atmosphere. The dispersion depends on the atmospheric refractivity model, including atmospheric conditions at the observatory site. The refractivity model of choice is Cassini's refraction model ([35],[38]), where the refraction R of a light ray meeting the atmosphere can be calculated using

$$R = \sin^{-1}\left(\frac{n_l r \sin z}{r+h}\right) - \sin^{-1}\left(\frac{r \sin z}{r+h}\right) \qquad (1)$$

where h and r are the height of the atmosphere and the radius of the earth respectively, z is the zenith angle, and n_l is the refraction index of the light ray at one wavelength. The wavelength dependency is found in the calculation for the refraction index, where the Lorentz-Lorenz equation is used to calculate the index depending on the atmospheric density, which is calculated using the CIPM-81/91 equation ([18],[30]). The refraction can be calculated for multiple wavelengths, with which the atmospheric dispersion can be calculated using

$$\Delta R_{atm} = \Phi(z)\left(n_l(\lambda_2) - n_l(\lambda_1)\right) \qquad (2)$$

with $\Phi(z)$ being a function similar to equation 1, depending only on the Zenith angle. In the ADC, the refraction of a prism with a small angle and located in a vacuum can be calculated using[35]

$$R = (n_g - 1)\phi \qquad (3)$$

where n_g is the refraction index and ϕ is the apex angle of the prism. For sets of two prisms with different apex angles, the dispersion for the prism set is known with

$$\Delta R_{ADC} = \Delta n_g(\phi_1 + \phi_2)\cos\theta \qquad (4)$$

where Δn_g is the difference in the refraction index of the prism material and θ is the optimal rotation angle of the prism. Born[35] suggests that equations 3 and 4 can be substituted and solved for the optimal prism angle

$$\theta = \cos^{-1}(c_f \tan(z)) \qquad (5)$$

where c_f is the filter constant, depending on the diameter of the primary mirror, the diameter of the ADC, the difference in refraction index for both the prisms and the atmosphere, and the apex angles of the prisms. The maximum velocity of the prism set is 110 "/s[34], which corresponds to 0.03 °/s. Typical simulations of the prism pair have a maximum duration of four minutes, which results in a rotation angle of ±4 degrees using the maximum speed and equation 5. The configuration of the prisms is shown in figure 2. Due to the accuracy with which the corrected light ray must intersect the detector, the tip- and tilt of the prisms must be $\gamma < 0.011°$. Furthermore, for the center of the prisms, it is required that the horizontal- and lateral shift $\delta_{xyz} < 50\ \mu m$.

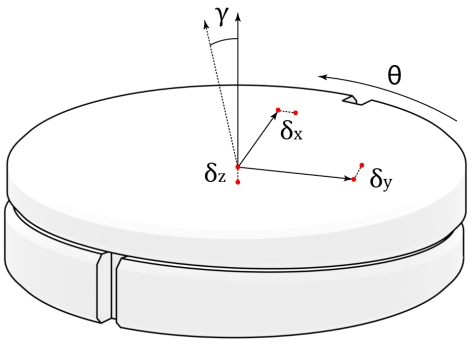

Fig. 2 Layout of the prism pair as deployed in the ADC.

2 Requirements

The requirements for the ADC originate from Zemax Opticstudio ray tracing simulations using equations from the previous sections, along with testing data of the current solution. In this chapter, the most essential requirements are given, yet more extensive arguments are given in Appendix A. During an observation, the ADC must be able to rotate with a maximum velocity of 110 arcsec/sec for a maximum duration of 240 s, resulting in a rotation angle of $\pm$ 4°. The initial angle of the prisms can be any depending on the observation, so the mechanism should be able to rotate to any starting position (360+ °). For the mechanism that is to be developed, it is assumed the prisms are in the starting position. The mechanism must hold two optical prisms, each with a mass of approximately 800 gr. Including a mount for the prisms, the mass will be approximately 2.5 kg. The prism-set center must not shift in the $x/y/z$ directions for more than 50 μ m. Furthermore, the light rays must not be obstructed by the mechanism, so a clear aperture of 100 mm is required in the center. Around this gap, a building volume with a radius of 150 mm and a height of 100 mm was agreed upon. The favored material is Aluminium 6061-T6 due to its well-known properties in a cryogenic environment, where a maximum stress of 150 MPa will be used to prevent any risk of metal fatigue. The mechanism must be fully compatible with a cryogenic environment in terms of thermal behavior, and hysteresis should be prevented to limit wear and thus high maintenance costs. The eigenfrequencies that do not resemble the intended motion must be higher than 70 Hz, and the mechanism must be able to endure an acceleration of $2.6G$ radially and $1.9G + 1G$ axially to resist earthquakes and shocks during transportation.

Based on the small deformation angle and the application in a cryogenic environment, this work concerns the development of a compliant mechanism that meets the aforementioned requirements (table 2). When using conventional rigid body joints inside a cryogenic environment, the use of a lubricant must be avoided. Therefore, dedicated parts are needed that are designed to endure the extreme environment. Even when using these parts, there will remain some hysteresis and wear in the joints. This often results in regular maintenance, which is undesirable in a large-scale cryostat that must cool down over a long period of time. Compliant mechanisms are void of any hysteresis or wear, which causes these types of mechanisms to have excellent repeatability. This also guarantees that no particle contamination will occur. Furthermore, these mechanisms generally have high resolutions, allowing for precise guidance possibilities in optical instrumentation.

Requirement subject	*Priority*	*Goal*
Deflection Range	3	Deflection range of the compliant mechanism must be at least $\pm 4^\circ$ or $\pm 0.02\pi$ rad.
Eigenfrequencies	3	Support eigenfrequencies must be at least 70 Hz, using both an infinite and absent actuation stiffness.
Thermal Center	3	The thermal center of the compliant mechanism must intersect the axis of rotation.
Payload	3	The compliant mechanism must rotate a mass of 2.5 kg located in the center.
Lifetime	3	The compliant mechanism must be able to operate for at least 10 years.
Actuator force	3	The total driving torque needed should not exceed 1 Nm.
Stress	3	The stress in the compliant mechanism should not exceed 150 MPa.
Center shift	3	The prism-set center point must not deviate more than 50 μm over the deflection range.
Acceleration	3	The compliant mechanism should be able to endure a maximum g-force of 2.6g radially and 1.9g + 1g static axially.
Design Volume	2	The compliant mechanism should fit within a volume with a diameter of 300 mm and a height of 100 mm with an optical aperture in the center having a diameter of 100 mm
Material	2	The preferred material of the compliant mechanism is Aluminium 6061-T6.

Table 1 List of Requirements. Priorities range from 1 to 3, where 3 means a fixed and 1 means a loose requirement

3 Compliant Mechanisms

A compliant mechanism is a flexible mechanism that achieves force and motion transmission through elastic body deformation rather than through rigid body joints. These elastic bodies are positioned to offer high compliance in directions where motion is intended and high stiffness in directions where motion is to be prevented. Therefore, these mechanisms often have an actuation stage in which the motion is fully governed by one or more elastic components, such that their kinematic operation is governed by stiffness properties only. A compliant mechanism intended for high precision is typically comprised of an actuation stage, flexure bearing system, actuator, sensor, and control strategy. The development of each of these components is dependent on the following metrics[1];

- Range of motion
- Degrees of Freedom (DoF), Degrees of Constraint (DoC) and overconstraints
- Parasitic motion
- Stiffness variation along the range of motion
- Critical vibration modes
- Thermal sensitivity
- Manufacturing sensitivity
- Hysteresis and creep
- Choice of sensors and actuators
- Choice of controller

In this research, the first five points are analyzed in detail, while taking the remaining data from the current solution of the ADC. Two configurations used in the design of flexure bearing stages are serial- and parallel kinematics. Serial designs can be achieved by stacking multiple single DoF systems to gain a large range of motion[8 19 31]. Such designs are often less complex to develop compared to parallel designs but suffer from moving actuators and cables which is a substantial source of disturbance. Parallel compliant mechanisms do not suffer from moving actuators but often offer a substantially smaller range of motion[3 6]. Parallel designs are developed by carefully choosing the constraints needed to achieve the intended motion. An example of a serial- and parallel setup is presented in figure 3. The elastic components of a compliant mechanism are called flexures. The flexure that will be extensively used in this work is the so-called leaf spring.

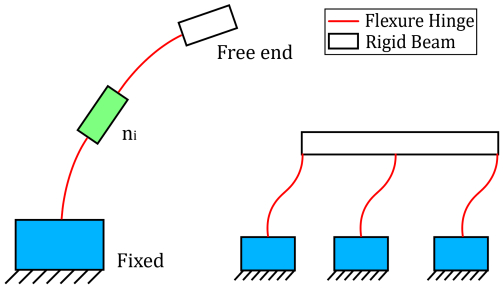

Fig. 3 Layout of a serial compliant mechanism which includes a number of intermediate bodies denoted with n_i (left), and a parallel layout where multiple connections to the fixed world are present.

3.1 Leaf springs

Leaf springs (other terms are sheet flexures, flexure blades, or flexure strips) are a common component of compliant mechanisms. The leaf spring often has a sub-millimeter thickness with a length and width that is orders of magnitude greater. The flexure offers high support stiffness in three directions while being compliant in the remaining three directions (figure 4). The latter directions in which compliance is deliberately maximized are called the Degrees of Freedom (DoF).

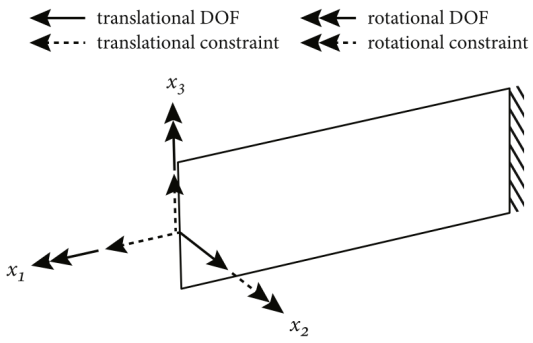

Fig. 4 Compliant- and Constraint directions of a clamped-free leaf spring[25]

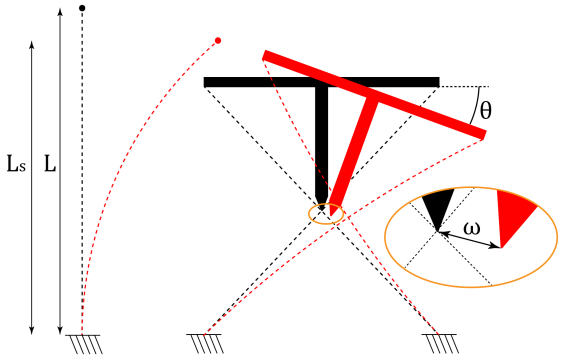

Fig. 5 Shortening of a leaf spring with length L to length L_s (left) and center shift ω of a cartwheel hinge under deflection angle θ (right)

While the flexure is often approximated with linearized stiffness or planar deformation, deformations are often sufficiently large such that disregarding non-linear effects is inappropriate. Large deflection of these leaf springs causes a decrease in lateral support stiffness, known as the elastokinematic effect. Therefore, the lateral stiffness must be evaluated over the entire range of motion. A second attribute of large deflections is the shortening effect (also called length contraction). A leaf spring with length L will have a decreased vertical length L_s when deflected (figure 5). At small deformations, the motion of single DoF rotational compliant mechanisms can be approximated as a circular rotation around a fixed axis. However, at larger deflections, this approximation is no longer valid as the trajectory of the motion deviates significantly from a circular path due to the nonlinearity of elastic deformations. The resulting parasitic motion is called center shift, which must not exceed the required maximum value of 50 μ m. In this work, the center shift will be defined as the deviation of the flexure motion compared to a circular trajectory. An example of a shortening leaf spring and center shift is presented in figure 5.

3.2 Design methodology

Thorough research has already been conducted to develop single Degree of Freedom compliant mechanisms. A list of existing designs is given in Appendix B. In this research, these designs are analyzed for their applicability in the specific case of the ADC. Deterministic behavior is established by using the principle of exact constraint design method Freedom and Constraint Topology (FACT)[12]. This method uses sets of Degrees of Freedom (Freedom Topology) and sets of System Topology (Constraint Topology). The combination grants the designer a visualization of the problem and a general shape that a viable compliant system concept must have in order to allow for specified motions. The FACT method uses Blanding's rule of complementary patterns, where it is stated that every freedom line intersects every constraint line[2]. The Freedom- and Constraint space of a single DoF rotational flexure is given in figure 6. The freedom space is represented by a single line, which is the rotation axis. The constraint space consists of planes intersecting this line in the center. Leaf springs must be placed inside the constraint space, to ensure that the system can make the motion given by the corresponding freedom (or rotation) space.

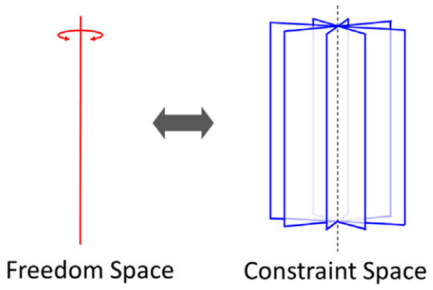

Fig. 6 Freedom space and Constraint space according to the FACT method[12]. Five non-redundant constraints must be chosen in the blue planes, intersecting the dotted line, which corresponds with the Degree of Freedom, given by the red rotation axis in the associated Freedom Space.

3.3 Flexible Multi-body Modeling Approach

While the FACT method gives the designer a clear indication of the behavior of the flexure, it does not yield any data regarding stress or stiffness. Flexible Multi-body Dynamics (FMBD) can be used for a more accurate indication of performance. FMBD utilizes "floating frames" to follow the mean rigid body motion of each element in a flexible beam. These elements are decomposed into rigid body motion onto which a sufficiently small deformation is superimposed. The finite element approach to kinematics and dynamics of flexible multibody systems uses an assembly of body elements interconnected at common nodal coordinates, where independent discrete deformation modes are applied. A set number of these modes is used for each finite element, characterized by a deformation mode coordinate. These coordinates are then expressed as a non-linear function of the nodal coordinates. Flexible joints can be considered slender one-dimensional components modeled by flexible beam elements. Manual implementation of these principles in each concept is possible yet cumbersome. Instead, this principle is applied in the program *SPACAR Light* which will be used extensively in this work.

3.4 Analytical possibilities

If one requires an initial estimate of flexure performance, approximations of the FMBD method are possible. To this extent, a common method that will first be described is the elliptic integral solution[40]. The method is elegant due to the exact solution of the Bernoulli-Euler equation, yet it is extensive and cumbersome to use in the initial phase of the design[13]. Research has also shown that the Adomian decomposition method can be used to model a beam with arbitrary boundary conditions. Although the method is relatively accurate, solving the ordinary- or partial nonlinear differential equations remains unsuitable for the initial design phase[20]. Lastly, the pseudo-rigid-body method (PRBM) can be applied[5 39]. This method approximates flexible elements with rigid beams and rotational joints, where each joint includes a spring constant. Although this method is less accurate, it provides an initial guess of displacement with relatively undemanding equations. However, when flexures consist of numerous leaf springs with unique geometries, all of the methods described above will result in both inaccurate and complex models, such that these methods will only be applied briefly in the early design phase to predict flexure behavior.

3.5 Simulations

The kinematic- and dynamic analysis of flexible multibody systems is applied in the program *Spacar*. *Spacar* can be used with *MatLab* and Simulink. *SPACAR Light* offers a more user-friendly port with Matlab, with ease of visualizing the results in a program called *Spavisual* including vibration- and buckling modes. The program uses numerical non-linear finite element theory for multi-DoF mechanisms[15]. Both planar and spatial mechanisms can be dynamically analyzed using flexible links. A perturbation method is used to solve the set of non-

linear equations of motion.
A clear distinction between rigid- and flexible bodies is made in *Spacar*. No flexible modes are included in rigid bodies, while in flexible bodies the designer can choose the modes that are of interest. These modes consist of elongation, torsion, out-of-plane bending, and in-plane bending respectively. Each beam element is programmed with two nodes and a connecting element as outlined in FMBD. Boundary conditions such as node fixing, displacements, and forces can be specified for each node using node properties, while material characteristics and flexibility are included in the element properties. It is not possible to simulate circular geometry in *SPACAR Light*. Therefore, each node of a potential circular shape N_i is approximated by a decagon using

$$N_i = [r\cos\left(\frac{\pi i}{6}\right), r\sin\left(\frac{\pi i}{6}\right)] \qquad i = [1:10] \tag{6}$$

where r is the radius of the circle and i is the number of nodes on the decagon. Because of the geometric limitations of the program, the results of the simulations will be verified using *Ansys Workbench* structural- and modal analysis where possible. When leaf springs are loaded in compression, an *Ansys* Buckling Simulation will be used to evaluate the critical buckling load. *Ansys* uses a general-purpose finite element algorithm to simulate meshes, allowing more organic geometry to be analyzed[17]. However, the simulations in *Ansys* are computationally far more expensive and more time-consuming. The modeling of compliant mechanisms in *Ansys* is not optimal because it does not function with a sketch-to-feature layout, which is why the software *SolidWorks* is used to develop all CAD models. Simulations of leaf springs in *Ansys* require an understanding of the meshing strategy to accurately simulate deflection behavior. The simulations use a large deformation algorithm, along with a fine mesh on the leaf springs to yield a realistic stress profile. For a guide to the *Ansys* setup, please consult Appendix C.

3.6 Optimization strategies

The optimization of a compliant mechanism is challenging due to the large number of variables, increasing with the complexity of the design. Even still, equations can be derived that expose which parameter changes have the most effect on countering unwanted behavior. Stress is linearly dependent on the length and thickness of the leaf spring(s) with

$$\sigma = \frac{M(x)}{2I}t \approx \frac{\theta E}{2}\frac{t}{L} \tag{7}$$

where $M(x)$ corresponds to the applied moment, I is the area moment of inertia, E is the module of Elasticity, and t, L are the thickness and length of the leafsprings respectively. To optimize stiffness behavior, the following equations are used

$$k_{\theta x3} = \frac{M}{\theta} = \frac{EI}{L} = C\frac{wt^3}{L} \tag{8}$$

$$k_{\theta x1,2} = \frac{M_{x1,2}}{\theta_{x1,2}} = \frac{GJ}{L} = C\frac{wt^3}{L} \tag{9}$$

$$k_{x3} = \frac{M_{x3}}{\theta_{x3}} = C\frac{w^3t}{L} \tag{10}$$

where $k_{\theta x3}$, $k_{\theta x1,2}$, and k_{x3} are the rotational-, pivot-, and lateral stiffness respectively (figure 4). G is the shear modulus, J is the St. Venant's torsion constant, and C is some material constant. Eigenfrequencies are evaluated using a free and fixed moving state. Actuators with high actuation stiffness such as piëzo's offer an approximately fixed moving state, whereas Lorenz-type actuators are simulated more accurately using a free moving state because the stiffness must be supplied by the controller. Numerical optimizations are possi-

ble using the non-linear optimization Nelder-Mead algorithm[22], where the maximum or minimum of an objective function can be found in a multidimensional space. However, usability decreases with the increasing complexity of the compliant mechanism due to the large number of variables. The maximum width and height are governed by the building volume, while the minimum leaf spring thickness is set to 0.2 *mm*, as this is the minimum thickness with which Wire EDM can be used with sufficient accuracy. The most realistic way to simulate the behavior of a flexure is to apply the force of the actuator at the same location and direction in the virtual environment. However, the specifics of the actuation are often unknown in the conceptual design phase. Therefore, the flexures will be simulated and optimized using three different actuation strategies described in the following paragraphs.

3.6.1 Torque

The first actuation strategy is to apply a torque load around the center point of the geometry. Using this strategy in *SPACAR Light* requires the presence of a node at this point. The simulation represents a perfect actuation strategy where the actuators cause a pure torque around the optical axis with a symmetrical design. Therefore, this strategy is used to determine the optimal leaf spring dimensions at the maximum actuation force with which the rotation angle is reached. Data is gathered regarding the stroke, stresses, center shift, and eigenfrequencies.

3.6.2 Forces

Another possibility is to apply radially symmetric forces around the origin of the design. As the actuation cannot be positioned in the center of the optical aperture, multiple actuators might be needed around the actuation stage. This type of simulation will therefore be more realistic than the pure moment around the center and can be used to determine the severity of center shift when the actuation forces are not uniform. This method can also be applied to find the optimal location and direction of the actuators.

3.6.3 Prescribed rotation

The final strategy involves a prescribed rotation around the origin. This can be seen as the inverse strategy of the torque load around the origin. Namely, a rotation is forced by the program, after which the engineer can see the stiffness and stress as a result of the deformation. In the event that the bending moment must be unreasonably high to reach the required deformation, this strategy can be consulted to investigate the cause.

3.7 Compounding

The static behavior and deflection range of compliant mechanisms can be greatly improved by compounding. The essence of compounding is to use multiple motion stages in series to enhance the deflection range of a system. The effect of leaf spring shortening (figure 5) can be cleverly compensated by allowing the leaf springs in separate stages to deflect in opposite directions. However, the downside of compounding is often a decrease in dynamic performance. The intermediate bodies (figure 3) are not connected to either the fixed world or the actuators. This makes the intermediate bodies of compounded compliant designs underconstrained and prone to vibrations, clearly reflected with low unwanted eigenfrequencies and unwanted Degrees of Freedom. Therefore, compounding can be a fitting solution if a large deflection angle is needed and low eigenfrequencies are tolerated for the application at hand. In this case, however, the unwanted eigenfrequencies must be 70 Hz at least.

3.8 Synchronizers

An example of the compounded linear guide consisting of four leaf springs is given in figure 7. As described in the previous section, the intermediate body has an unwanted (translational) Degree of Freedom δ_{int}. In the upcoming sections, all illustrations have their fixed, intermediate, and actuation bodies indicated with blue, green, and white respectively. Panas, Hopkins[26] suggests that an intermediate body can be kinematically coupled to the actuation stage through an external linkage (also called a synchronizer), such that both static- and dynamic behavior can be improved by compounding. Any effective synchronizer design must be attached to all rigid bodies. The design of the synchronizer must have a minimized stiffness in the intended DoF direction, while specifically maximizing the stiffness in the direction of the unwanted DoF. In figure 7, the lever is the synchronizer which allows the intended motion of the mechanism while restraining the intermediate body from moving independently. A new design challenge arises to develop the synchronizer without the introduction of conventional joints. The synchronizer can be seen as a compliant mechanism itself, and will therefore be optimized separately as well as connected to the main stage. The development of compounded synchronized compliant mechanisms brings to light the relative difficulty in analyzing and designing compliant mechanisms[13].

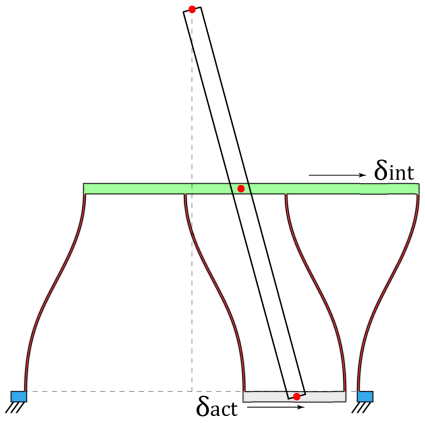

Fig. 7 Synchronizer design of a compounded linear guide. The lever forces the intermediate body to move approximately half as much as the actuation stage $\delta_{act} \approx 2\delta_{int}$. The lever eliminates the unwanted Degree of Freedom, which is the translational movement of the (green) intermediate body.

3.9 Contributions

While the state-of-the-art solutions found in the literature research provide a foundation for the mechanism development, a fundamental design approach was required to obtain suitable concepts to fit the requirements. The following pioneering contributions are offered by means of this process;

- Alteration of existing compliant mechanism designs to meet the requirements of astronomical instruments.
- Use of a fundamental design approach to introduce compliant mechanism designs not found in the literature research.
- Optimization of multi-variable mechanisms using the software SPACAR Light and ANSYS Workbench.
- The introduction of a coupling device called a synchronizer to reduce the dynamic penalty of serial motion stage addition.

4 Concepts

As mentioned in section 3.1, a leaf spring offers three constraint- and three compliant directions. This section offers numerous geometrical combinations of these leaf springs to obtain design concepts that meet the requirements.

A leaf spring can be adapted to have two constraints with high compliance in all rotational directions. This is done by including a notch (figure 8a). As can be seen, the design now includes a normal leaf spring and a notched leaf spring, having a total of five constraints. The (white-colored) actuation stage θ_{act} has six possible directions of motion, namely three translations and three rotations (figure 4). Five of these directions are constrained by the design, and only the rotation around the virtual axis where the leaf springs meet is allowed according to the FACT method described in section (3.2). Therefore, this design is considered to be exactly constrained.

While there are numerous advantages to such an exactly constrained design, precision mechanisms are often deliberately overconstrained (that is, more constraints are present than required to obtain the required DoF). This is done to enhance certain characteristics such as thermal behavior and stiffness. The present example can be adapted to obtain radial symmetry with a triple leaf spring configuration (figure 8b). When the leaf springs expand due to large temperature differences, the rotational axis of example figure 8a will shift while the rotational axis of figure 8b stays in the same position.

The second consideration is the addition of multiple motion stages in series as described in section (3.7). During the initial testing phase of this research, it became evident that the required deflection range cannot be reached in the required design volume without compounding. The present example is displayed in a compounded configuration in figure 8c, resembling a renowned cartwheel hinge with the addition of an intermediate body.

This chapter aims to present several combinations of radially symmetric and compounded designs that fit the required volume of this research. Each concept is optimized using the method described in section 3.6, and the final performance is presented.

4.1 Cartwheel Hinge

The principle of compounding is first explored as a serial expansion of the previous concept (figure 8). A second layer of leaf springs is added on top of the introduced intermediate body, increasing the deflection angle at the same actuation force with lower stress levels in the leaf springs. The design is now similar to the renowned Cartwheel Hinge[16 29]. Paros[28] did pioneering research by analyzing critical spring rates, after which the concept was widely used in precision mechanisms. The design is not complex and the performance can therefore be derived with analytical equations found in literature. Kang[16] compared the analytical model of the cartwheel hinge to the performance of subsequent FEM models, resulting in a maximum error of 10%. However, the applicability of this theory is brought into question with the newly introduced intermediate body which can rotate freely while the actuation stage is fixed by the actuator, revealing an unwanted Degree of Freedom.

4.1.1 Results

After optimization, a deflection angle of $\pm 4^\circ$ can be achieved at the maximum actuation force with an out-of-plane support stiffness of $K_z = 2.46 \cdot 10^6$ N/m and a stress of 51.5 MPa. When a pure moment is applied at the actuation stage, Kang[16] suggests the normalized center shift ω_d can be approximated with

$$\omega_d = \frac{\theta^2}{30 \cos \alpha} \tag{11}$$

where the commonly used angle $\alpha = 45^\circ$ is applied (figure 8). The difference between the analytical approximation and the simulation result shows that the optical aperture drastically increases the center shift, making the design unusable (figure 10). Furthermore, the absence of radial symmetry makes the design thermally unstable.

4.2 Butterfly

The effect of center shift is minimized in the rotational compliant mechanism design called the Butterfly hinge[11 23], which can be thought of as a compounded cartwheel hinge. Typical applications of this design found in the literature review include inter-satellite communication systems and optical scientific instruments. The geometry is investigated in two configurations, either fixing two bodies or a single body (figure 9). By fixing two bodies, radial symmetry is achieved and the center shift is eliminated entirely. Moreover, compounded radially symmetric systems are considered the most thermally stable. This is due to the fact that the compounded stages can expand and retract without causing a shift in the prism location or stress in the leaf springs. However, deflection angles can be greatly increased by fixing only one body at the cost of dynamical performance and thermal behavior.

4.2.1 Results

The double-clamped butterfly concept can deflect $\pm 4^\circ$ at the maximum actuation force with a leaf spring thickness of 0.362 mm. The need for a relatively thin width of the leaf springs can be explained by the reduced length of the leaf springs, limited by the position of the intermediate bodies. The support stiffness in the out-of-plane direction is $K_z = 6.34 \cdot 10^6$ N/m with a stress of 65.1 MPa at maximum deflection. Modal analysis of the design revealed two unwanted Degrees of Freedom, exposed by low eigenfrequencies. Both intermediate bodies can vibrate around the pivot point with an eigenfrequency of approximately 30 Hz. The design is considered unsuitable for this application because multiple unwanted eigenfrequencies were detected. Furthermore, the position of the actuation stage relative to the intermediate body complicates the development of a synchronizer as described in section 3.8.

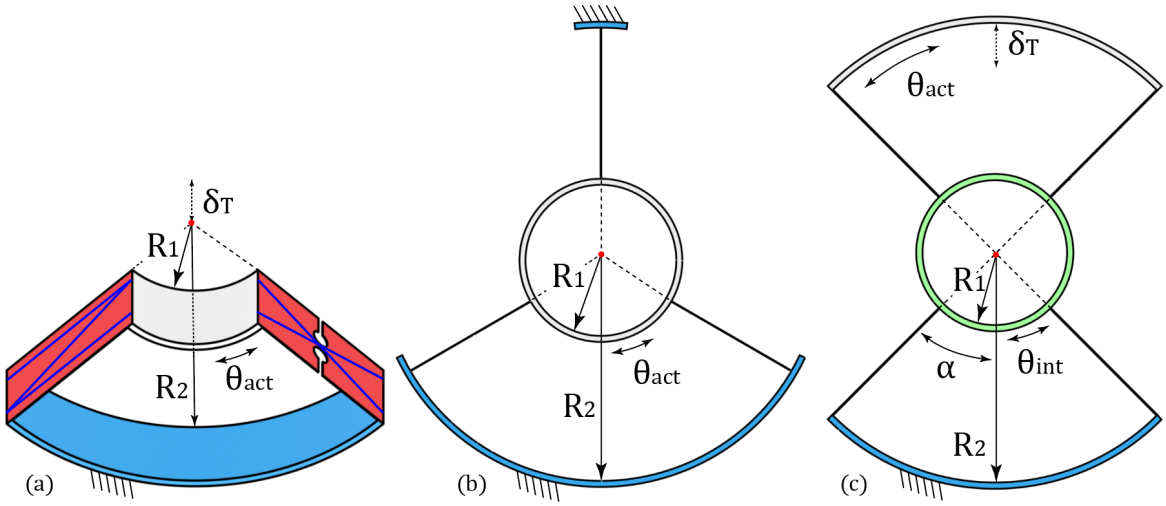

Fig. 8 Rotational compliant mechanisms in a (a) exact constraint, (b) parallel radially symmetric, and (c) serial configuration.

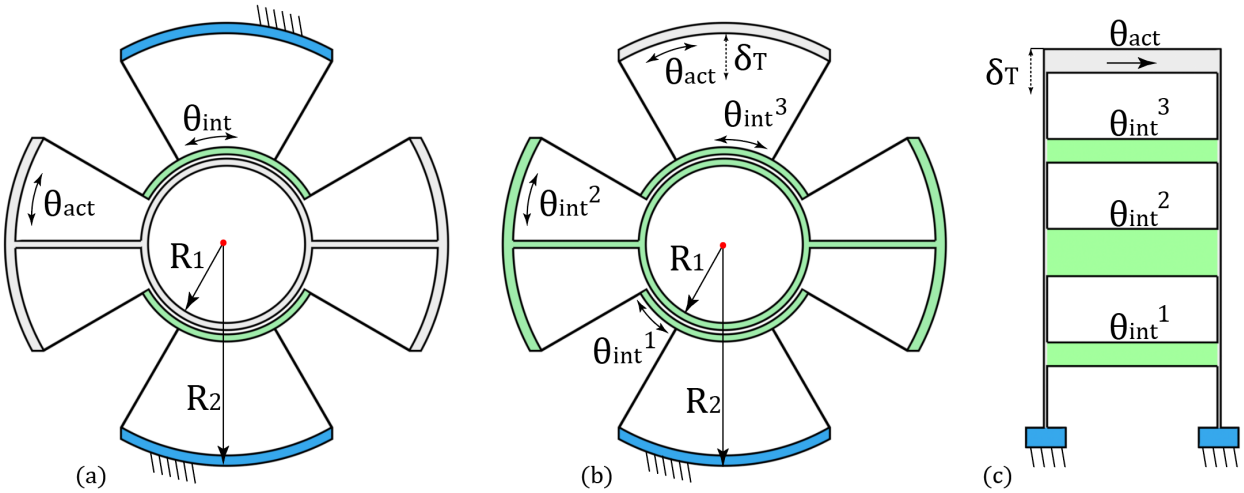

Fig. 9 Butterfly in a (a) radially symmetric or (b) serial configuration. The serial configuration consists of three intermediate bodies visualized in (c).

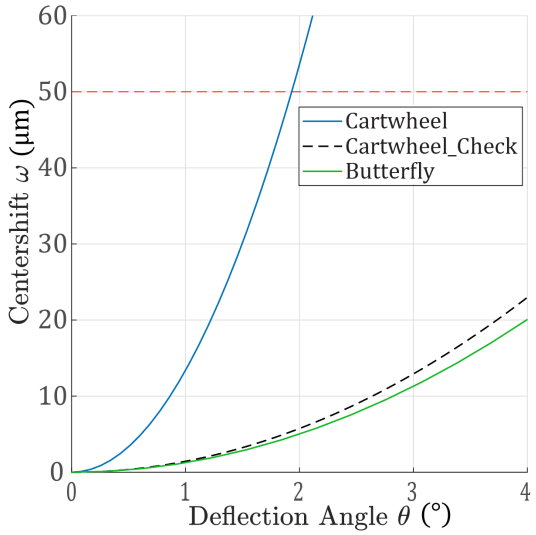

Fig. 10 Center Shift of the Cartwheel and Butterfly without radial symmetry. The Cartwheel center shift was also determined analytically.

The second configuration of the butterfly hinge has only one fixed body. This concept can deflect $\pm 4^\circ$ at the maximum actuation force with a leaf spring thickness of 0.590 mm. The support stiffness in the out-of-plane direction is $K_z = 1.22 \cdot 10^6$ N/m with a stress level of 42.4 MPa at maximum deflection. The center shift of the actuation stage is low enough for this application due to the compensation caused by the compounded stages (figure 10). However, the design is still considered thermally unstable due to the lack of radial symmetry. Modal analysis of this configuration revealed three unwanted Degrees of Freedom with eigenfrequencies of 16, 63, and 65 Hz respectively. A simplification of this serial configuration is shown in figure 9. If one imagines to fix the actuation stage, intuitively, all three bodies could still move independently. Because of poor dynamical performance in combination with thermal instability, this design is considered unsuitable for this application.

4.3 Large Angle Flexure Pivot

Numerous radially symmetric compounded monolithic designs were explored (figure 11), the most noteworthy being the Large Angle Flexure Pivot (or LAFP)[32]. The mechanism is especially adequate for applications where a large stroke is desired. The stroke of the original design can reach $\pm$ 180°, and infinite operational lifetime is achieved using a stroke of $\pm$ 70°. The application was the angular guidance of an optical component in a space (or cryogenic) environment[32]. The inner ring denoted by the radius R_1 consists of three separate intermediate bodies, connected by linear guides with length L_{lin}. These linear guides allow the major leaf springs with length L to shorten because the three intermediate bodies can expand and contract under deflection, giving thermal stability to the system. Therefore, these three bodies must not be rigidly linked together. As one can imagine, the inner radius will increase slightly while going through the range of motion as a result of shortening. These intermediate bodies must rotate approximately half the angle of the actuation stage, on which the prisms will be mounted. The model has now increased in parameters to the limits of what *SPACAR Light* can analyze (For further details, please consult Appendix D, F). Although experiments were done using an updated version of the software, the development was limited by the capabilities of *SPACAR Light*.

4.3.1 Results

It is clear that a stroke of $\pm$ 4° can be reached with abundant lateral stiffness ($1.62 \cdot 10^6$ N/m) at maximum deflection and no center shift due to leaf spring shortening. Optimization of the leaf spring thickness to reach the required deflection at maximum actuation force yields 0.495 mm for the main leaf springs and a linear guidance thickness of 0.35 mm. The stress in the material at maximum deflection is 44.6 MPa.

While the kinematics of this design are sufficient by a large margin, dynamical behavior is compromised due to the presence of three intermediate bodies. However, modal analysis reveals only one unwanted degree of freedom. Because all kinematic requirements are met, and only the first unwanted eigenfrequency is below the required 70 Hz, an angular symmetric synchronizer as described in section 3.8 will be developed to improve dynamic performance.

4.4 Compounded Torsion Pivot

Another possibility is explored using a non-monolithic design approach where the leaf springs are arranged axially. The leaf spring length is now bound by the height of the design volume, and horizontal center shift is absent due to radial symmetry[10]. Brouwer[4] suggests that the cross-section of a free leaf spring loaded in torsion does not inhibit a uniform displacement, but has a distribution in the longitudinal direction. This effect of non-redundant displacement due to shear stresses in the cross-section is called warping. The non-compounded version of this design is purely parallel, meaning that no unwanted Degree of Freedom can be present. However, this design is ill-equipped for the ADC due to vertical prism shift caused by leaf spring shortening.
Warping can be reduced by foreshortening the leaf-springs[10] as shown in the adapted design in figure 12. To reach equal foreshortening along the width of the leaf springs, a parabolic curve is required using the equation

$$\delta(r) \cong \frac{3(r\theta)^2}{5a} \tag{12}$$

However, when optimal bending stress is desired over the width of the blades, the following equation determines the geometry

$$\sigma(r) \cong \frac{3Et(r\theta)}{L^2} \tag{13}$$

where a is the height of the leaf springs, L is the length of the leaf springs, r is the radius of the mechanism, θ is the deflection range, t is the leaf-spring thickness, and E is Young's modulus. The compromise often used in literature is to join the leaf springs to conical end caps, called tapering (figure 13).

These equations suggest that a large ratio of height to width will increase performance. Tapering is applied to the leaf springs with an optimal angle of approximately 5.5° calculated using equation 13, verified using *Ansys* simulations (figure 14).

Without tapering and for limited deflection angles ($< \pm 2^\circ$), *SPACAR Light* and *Ansys* seem to agree with the results. However, larger deformations yield substantial differences due to a linear dependency of the applied moment and the torsion angle used in *SPACAR Light*. Therefore, where monolithic designs can be verified using both *SPACAR Light* and *Ansys*, the torsion pivot is only analyzed using the latter. Note that other than the unavoidable differences between both software packages, all data regarding materials, masses, loads, and supports are kept the same.

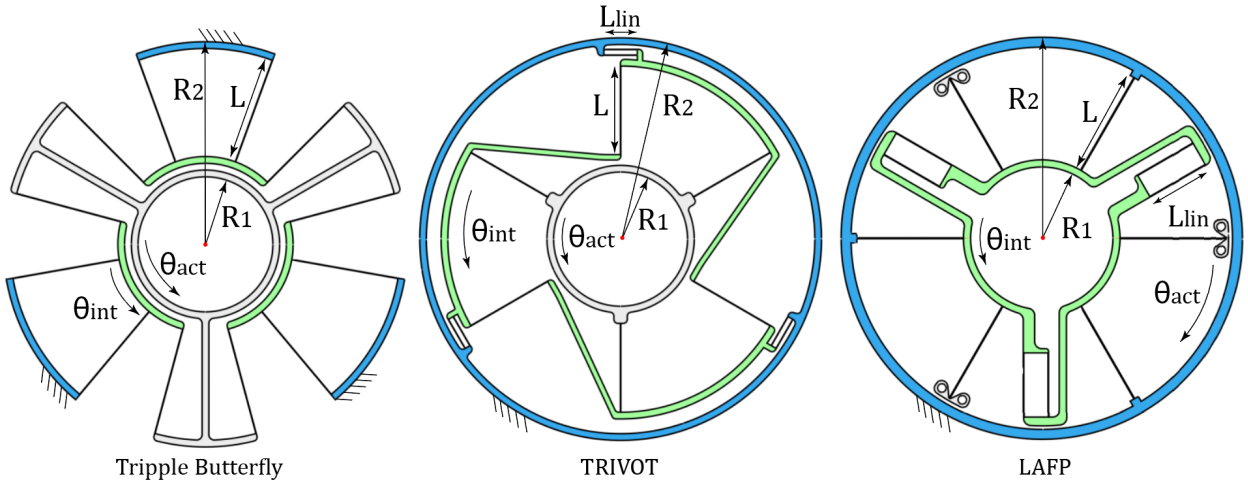

Fig. 11 Three radially symmetric compounded compliant mechanisms. The Triple Butterfly (left), TRIVOT (middle), and LAFP (right).

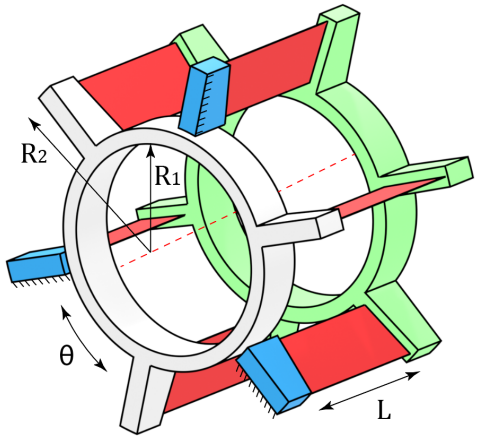

Fig. 12 Design of a Compounded Torsion Pivot flexure. The red planes indicate the position of the leaf-springs and the blue surface indicates the clamped plane.

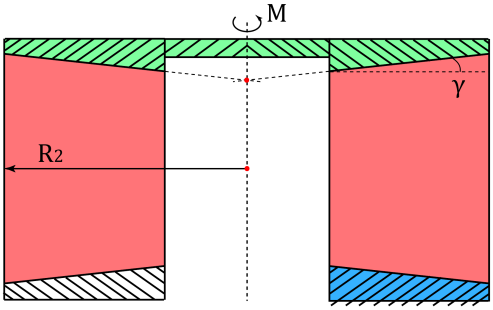

Fig. 13 Cross-section of the CTP design. Tapering of the leaf springs is indicated with angle γ.

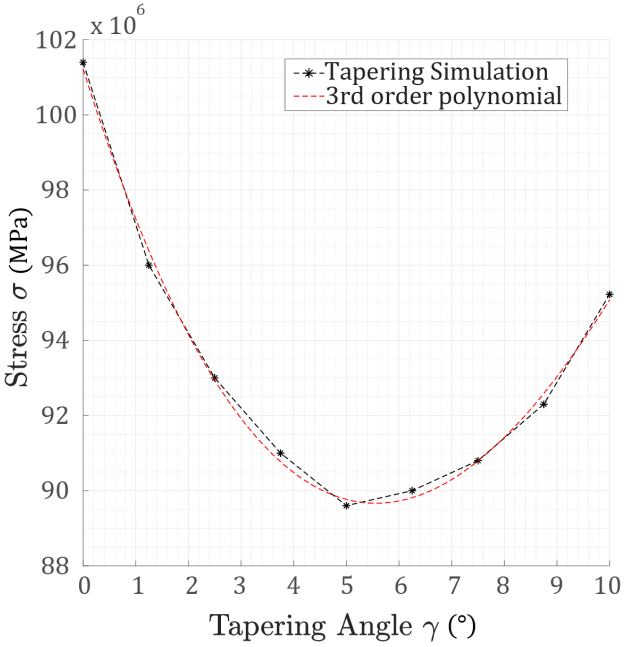

Fig. 14 Stress evaluated under increasing shortening angles simulated using Ansys.

The mass of the payload can cause a sudden drop in the support stiffness of the flexure, otherwise known as buckling. Stiffness equations for a leaf-spring prone to buckling are widely known, but if the tapering angle is increased, normal beam theory becomes invalid[10]. Therefore, buckling will be evaluated using *Ansys* and an analytical approximation using a rectangular leaf spring. The critical load $N_{x,cr}$ can be verified for a single leaf spring using

$$N_{x,cr} = -\frac{k_c \pi^2 E t^3}{12L^2(1-\nu^2)} \tag{14}$$

where a is the loaded plate length, h is the thickness of the plate, E is the Elastic Modulus, ν is Poisson's Ratio, and k_c is the Critical Buckling Coefficient[14]. The analytical approximation yields a critical buckling load of 261.7 N/m. The critical buckling load according to *Ansys* simulations is 380.7 N/m. The large difference is caused by the analysis of a single non-tapered leaf spring using the equation multiplied by three instead of analyzing the system as a whole in *Ansys*. Nonetheless, the buckling multiplier is in both cases larger than 10, which is the minimum value required at Astron Nova.

4.4.1 Result

Simulations show that a rotation of $\pm$ 4° is possible with the maximum applied moment, along with a high support stiffness ($6.12 \cdot 10^5$ N/m), and sufficiently low stresses (89.5 MPa). These results were achieved using a leaf spring thickness of 0.41 mm. The vertical shift of the prisms is avoided by using a compounded design. While the kinematic requirements were met, the dynamics are lacking with one low unwanted eigenfrequency of 14.84 Hz corresponding to the rotation of the intermediate body. In order to increase the eigenfrequency and meet the dynamic requirement, a synchronizer is developed to couple the intermediate body to the actuation stage.

4.5 Optimization Example and Results

The analysis of the previous sections can be visualized by a comparison between all concepts. This is presented in terms of kinematic- and dynamic performance on the following pages (figure 16, table 2). The data is obtained using *SPACAR Light*, and the monolithic designs are verified with *Ansys*. Frequency behavior in the deflected state is obtained using *SPACAR Light* only. The method used to obtain the optimal geometry of the concepts is presented for the LAFP below. Please note that each concept has been optimized using the same steps.

4.5.1 LAFP optimization

The length and width of the leaf springs are maximized in *SPACAR Light* using the node equations given in Appendix F. These are bound by the maximum design volume stated in the requirements. Once the model is created, the leaf spring thickness is varied to obtain enough deformation. This is done for all load cases described in section 3.6. Critical values such as stress and stiffness are then evaluated (Figures 15a,15b). Each variable is optimized to allow sufficient deflection while keeping within the required performance characteristics. Each optimization is then checked in terms of performance using *Ansys Workbench*. Optimization algorithms like the Nelder-Mead method are not applied due to the large number of variables which are optimized individually instead. The author of this research recognizes the improvements that can be made in this area, which is therefore recommended as future research. As a result, there can be no statement that the resulting design has fully optimized performance, only that the performance is sufficient for the stated requirements.

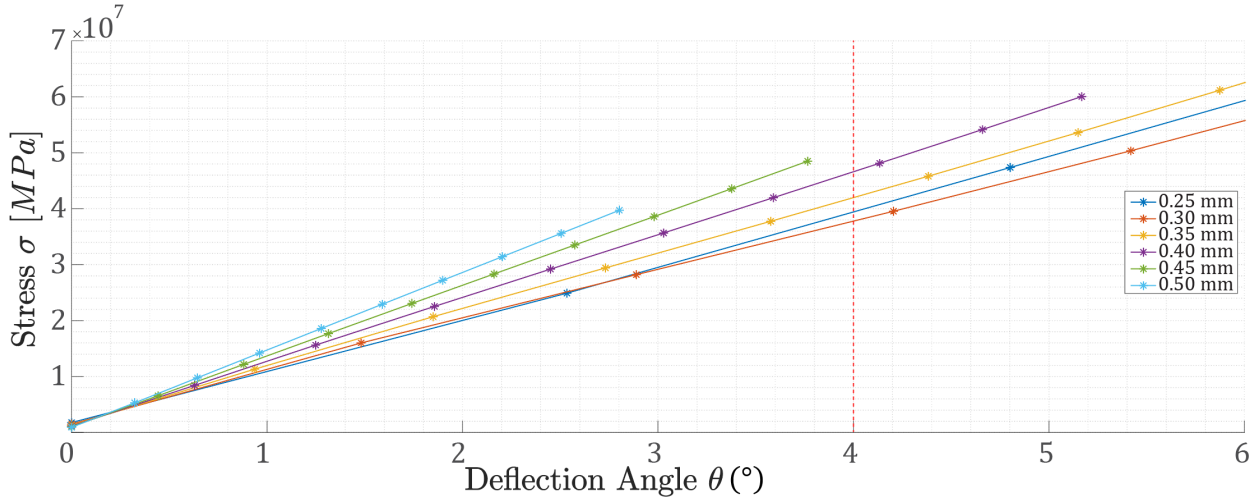

(a) Stress Optimization of Leaf Spring Thickness

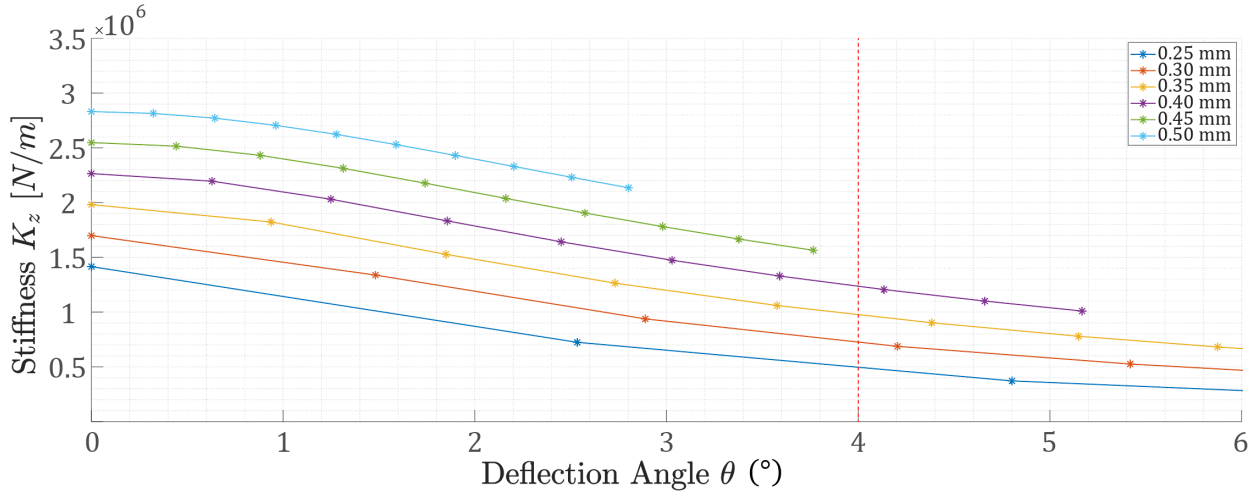

(b) Support Stiffness Optimization of Leaf Spring Thickness

Fig. 15 Optimization method

Concept	*Leafspring Thickness*	*Support Stiffness*	*Stress*	*Unwanted Modes*
Cartwheel	0.575 mm	$2.46 \cdot 10^6$ N/m	51.5 MPa	1
Serial Butterfly	0.590 mm	$1.22 \cdot 10^6$ N/m	42.4 MPa	3
Hybrid Butterfly	0.362 mm	$6.34 \cdot 10^6$ N/m	65.1 MPa	2
Triple-Butterfly	0.370 mm	$7.93 \cdot 10^6$ N/m	54.9 MPa	3
TRIVOT	0.430 mm	$0.51 \cdot 10^6$ N/m	77.5 MPa	2
LAFP	0.495 mm	$1.62 \cdot 10^6$ N/m	44.6 MPa	1
CTP	0.405 mm	$0.61 \cdot 10^6$ N/m	89.5 MPa	1

Table 2 Performance of each concept. Please note that these statistics are achieved with the application of the maximum actuation force to reach the required deflection angle.

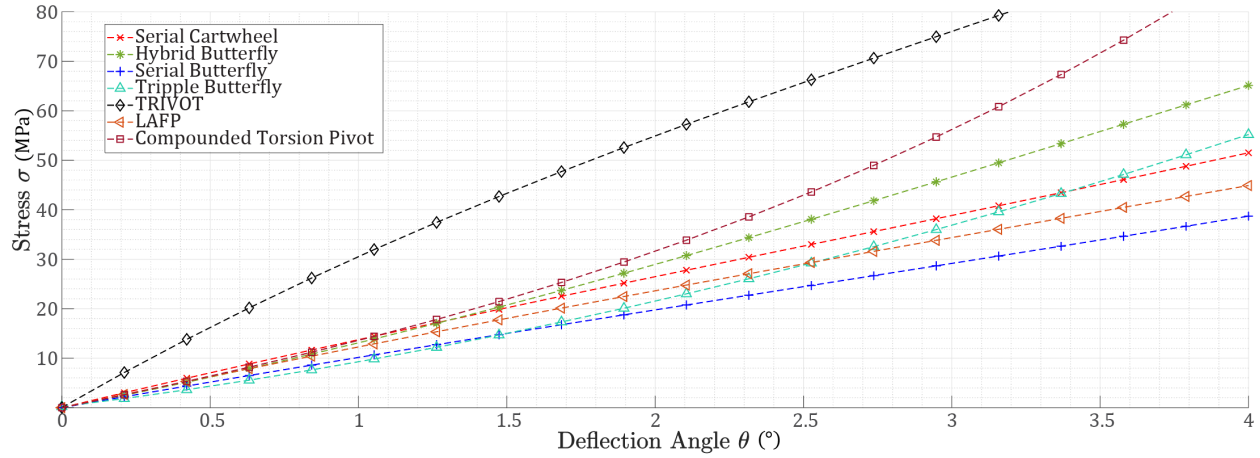

(a) Stress

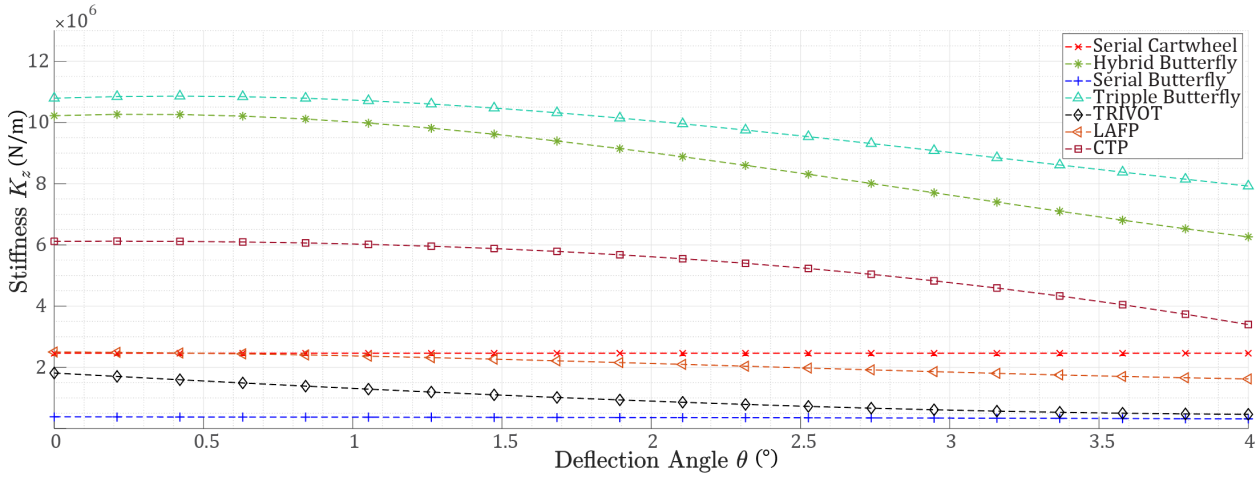

(b) Support Stiffness

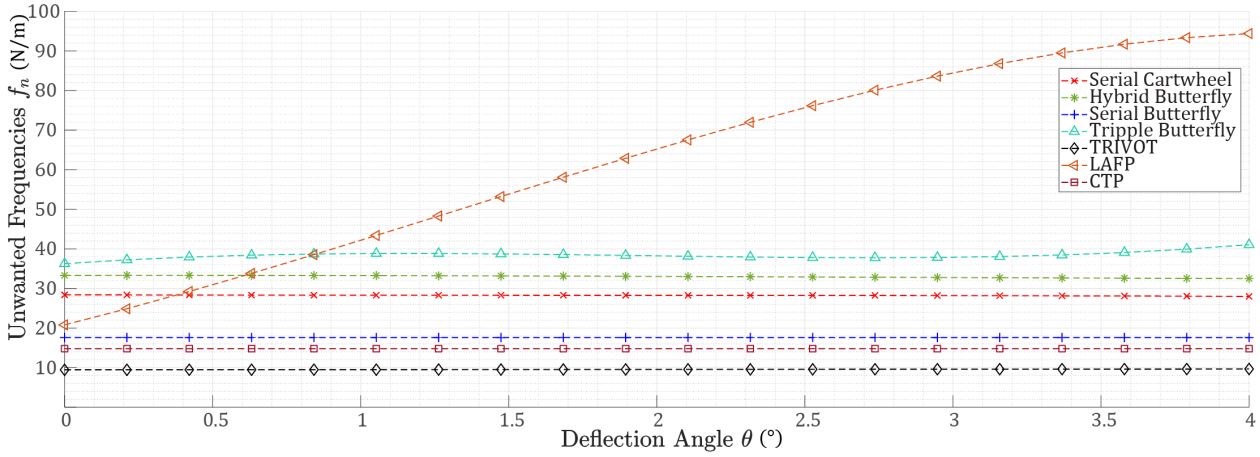

(c) Unwanted Frequencies (Lorenz-type actuators assumed)

Fig. 16 Comparison between the concepts analyzed in this thesis.

5 Synchronizer Design

From the previous section, it is clear that compounding is needed to obtain enough deformation using the maximum actuation force. However, the introduction of compounding makes the designs underconstrained. Underconstraints are exposed in the modal analysis by low eigenfrequencies and resemble unwanted Degrees of Freedom. Two compounded compliant mechanisms of the previous section only had one unwanted Degree of freedom, namely the Large Angle Pivot Flexure and the Compounded Torsion Pivot. This section aims to resolve the unwanted Degree of Freedom with the development of a synchronizer as described in section 3.8.

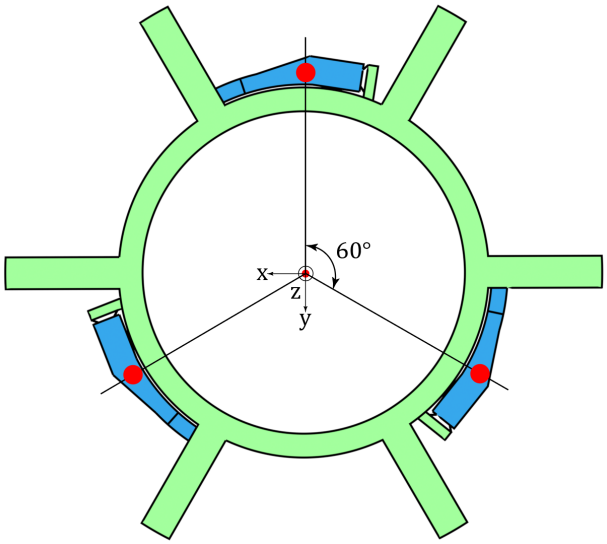

Fig. 17 Top view of the synchronized Compounded Torsion Pivot. The blue body represents the position of the synchronizer. Each synchronizer is positioned radially around the origin in the "dead space" of the design.

5.1 Compounded Torsion Pivot Synchronizer

The development of a synchronizer for the CTP (figure 12) is not found in the literature. However, this thesis suggests that a similar approach as deployed in section 3.8 can be applied. The position of the synchronizers is in the "dead space" of the design, meaning no extra design volume is needed. This is visualized with a top view presented in figure 17. A side view of the CTP is given in figure 18 along with a lever design that couples the stages together. To account for the rotational motion of the synchronizer in multiple directions, the lever must also allow a rotation around the $z-axis$. This is done by applying a set of pivot flexure hinges to attach the intermediate body and actuation stage. However, the pivot point must remain a single pivot flexure to prevent any vibration of the synchronizer body denoted with n. Three of these lever systems are positioned radially around the optical axis.

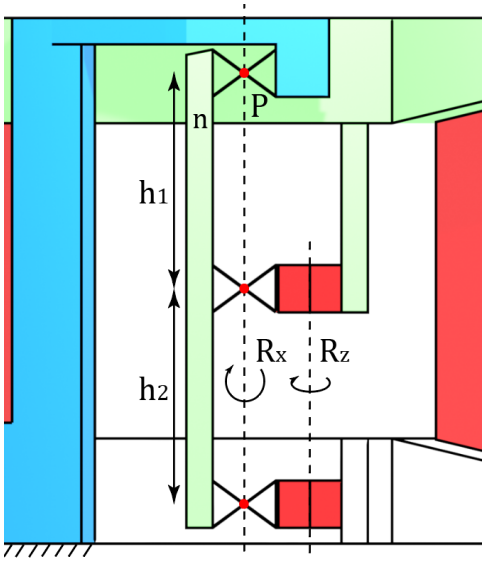

Fig. 18 Side view of the synchronizer design for the CTP. The synchronizer body n forces the movement of the intermediate body (green), and the actuation stage (white) with a rotation around the pivot point P.

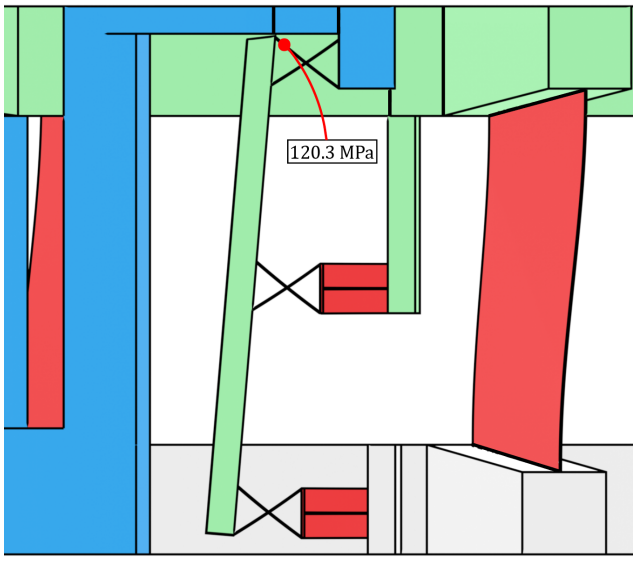

Fig. 19 Maximum stress at maximum deflection of the CTP synchronizer.

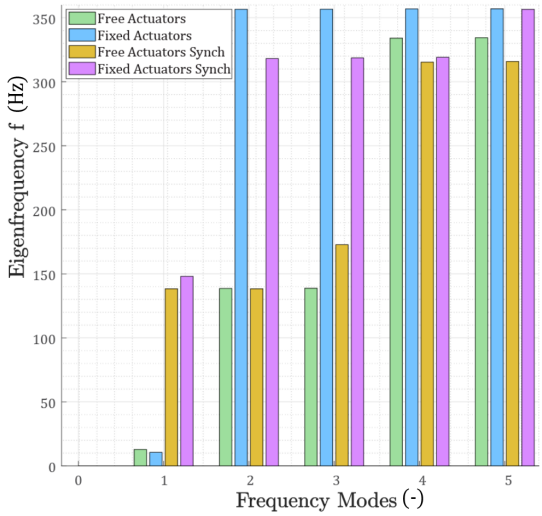

Fig. 20 Unwanted eigenfrequencies of the CTP design, including differences using an infinitely high or absent actuation stiffness.

5.1.1 Kinematics

The stress in the material at $\pm 4^\circ$ of deflection is 130 MPa, which is below the maximum allowed stress (figure 19). However, stress increases rapidly with increasing deflection angles. The length of the lever must be maximized to limit the rotation in the pivot point P but is constrained by the maximum height of 100 mm. Thus, the performance will likely increase substantially when the building height is increased. The thickness of the flexure pivots is 0.2 mm, which is the minimum thickness that can be produced using Wire EDM. The lateral stiffness when a synchronizer is included is reduced to $4.04 * 10^6$ N/m under full deflection. While this is in the acceptable range, the steep decrease in support stiffness with an increasing deflection angle is notable with this design (figure 14b).

5.1.2 Dynamics

The first unwanted eigenfrequency is increased from 14.8 to 138 Hz when simulated without actuation stiffness. Full data on the frequency behavior is presented in figure 20. A modal analysis of the deflected state using Ansys is presented in Appendix G. While this design does meet the requirements of this work, producibility is questionable due to the thin leaf springs found in the synchronizer. Moreover, the stress in the leaf springs is breached when the deflection angle is increased to $\pm 4.5^\circ$, limiting the lifetime of the mechanism.

5.2 Large Angle Pivot Flexure Synchronizer

The introduction of a lever system as suggested in the CTP synchronizer is not possible due to the optical aperture in the center of the LAFP. Another lever system can be directly used as presented in figure 21. The figure represents one of the three synchronizers, deployed in a radial symmetric manner similar to the CTP. Five pivot points are introduced using flexure pivots. While the frequency can be increased to 70 Hz in this manner, the design volume is breached. The mode corresponding to this frequency is a vibration of the synchronizer itself. Furthermore, the LAFP is no longer monolithic when applying this synchronizer on top. Therefore, the challenge is to develop a better-performing

synchronizer without compromising the design volume. Similar research was done by Hopkins[26], utilizing a circular flexure to couple the design of a compounded linear guide without extending the geometry to the pivot point. Inversely, the addition of a linear guide as the linkage is beneficial in a circular flexure design. One elegant solution found in the literature is presented in figure 22.

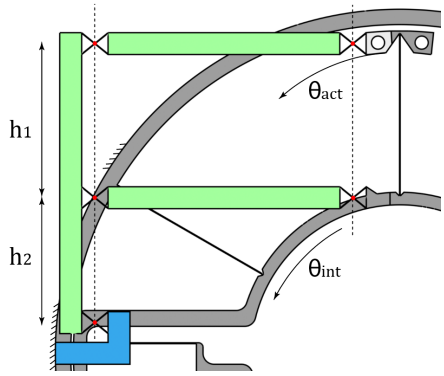

Fig. 21 Original concept of the LAFP synchronizer design. The synchronizer is placed on top of the LAFP design and attached to the blue- and white sections. The main LAFP is greyed out for clarity. Optimal synchronization was met when $h_2 \approx 0.7h_1$

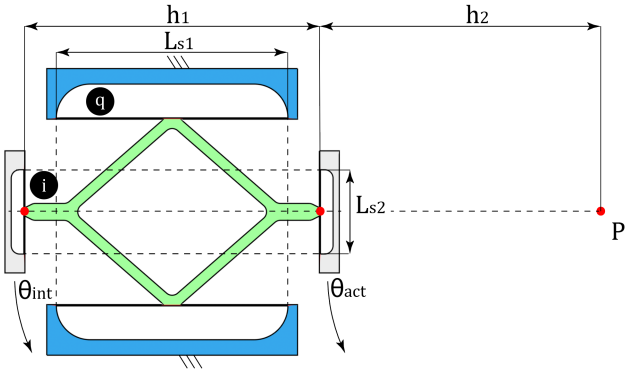

Fig. 22 Synchronizer design coupling an intermediate body θ_{int} of a radial design with a linear guide to the actuation stage θ_{act}. The intermediate body and the actuation stage move an equal amount vertically but at a different distance from the pivot as long as $h_1 = h_2$.

As long as the distance from the intermediate body to the actuation stage h_1 is identical to the distance from the actuation stage to the origin h_2, the actuation stage is moved approximately twice as much as the intermediate stage by the linear guide flexures indicated with q. Both stages allow for some movement in the normal direction by the flexures indicated with i, allowing the linear guide of the LAPF main stage (figure 11) to remain functional. The intermediate body must be able to shift toward the pivot point. Kinematically, the equivalent of this synchronizer is given in figure 23. When applied to the geometry of the LAPF, one glaring obstacle is that the position of the respective stages used in Hopkins is flipped around (figure 24)[26]. These stages cannot be inverted in the main LAPF design because the three intermediate bodies would be heavy and thus dynamically underperforming. In his work, an external rigid linkage is suggested to invert the stages for the synchronizer.

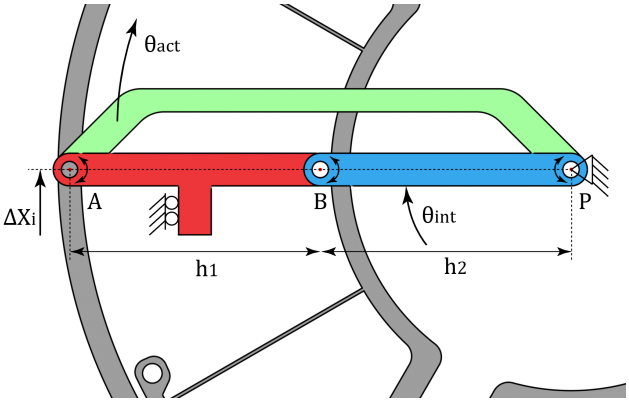

Fig. 23 Kinematic visualization of the LAFP synchronizer. The red body can translate upwards, forcing a uniform movement Δx_i on both θ_{int} and θ_{act}. However, since the distance AP (with $h_1 = h_2$) is twice the distance of AB, the desired synchronization is achieved.

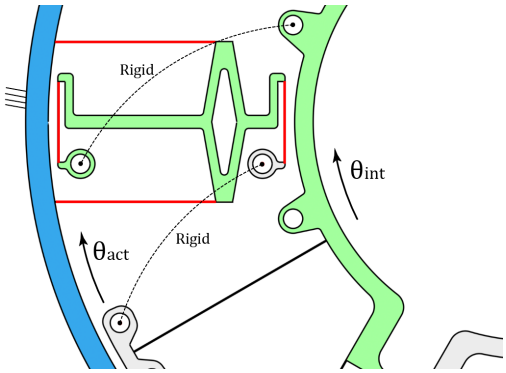

Fig. 24 Inverted stages of the LAPF monolithic synchronizer design. The dotted lines indicate the connection points for which an external rigid connection is required.

5.2.1 Kinematics

To reach the required rotation at the same actuation force, the six leaf springs of the main stage with length L need to be thinner (0.30 mm), and the optimal linear guide leaf spring thickness with length L_{lin} is reduced to 0.24 mm. Lateral stiffness when using a synchronizer is reduced to $5.9 \cdot 10^6$ N/m at maximum deflection, with a maximum stress of 103 MPa, located in the introduced linear guide (figure 27). While it is clear that a synchronizer dramatically improves the dynamical performance of the LAPF, larger deflections in the range of $10-15^\circ$ are not possible with the current solution due to this increasing stress.

5.2.2 Dynamics

The introduction of the synchronizer causes the first unwanted eigenfrequency to be 132 Hz for free actuators and 200 Hz for fixed actuators as shown in figure 26. However, the synchronizer limits the deflection range due to the linear guide, which must deflect approximately the same amount as the major leaf springs of the LAPF concept. A modal analysis of the deflected state using Ansys is presented in Appendix G. While the requirements of this work are met, a synchronizer design to couple intermediate stages while allowing relatively large ranges of motion is not achieved and seems like an opportunity for future studies. Due to the monolithic nature of the design, the production of the synchronized LAFP is possible using a combination of milling and Wire EDM. The final CAD model of the LAFP including the synchronizer is presented in figure 25. A 3D-printed prototype was made out of PLA using Fused Deposition Modeling. The leaf spring dimensions of the prototype are changed for demonstration purposes (figure 28).

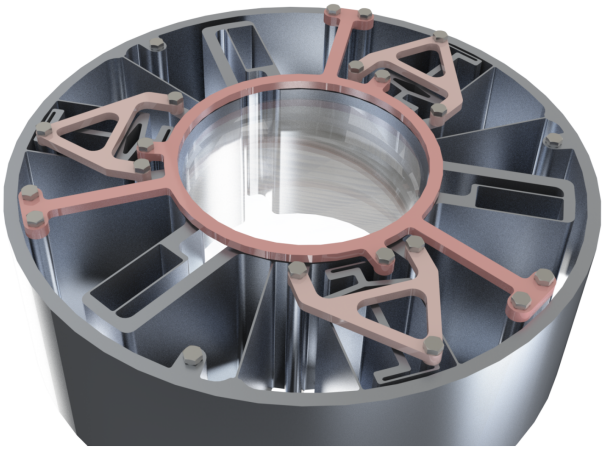

Fig. 25 CAD model of the final concept

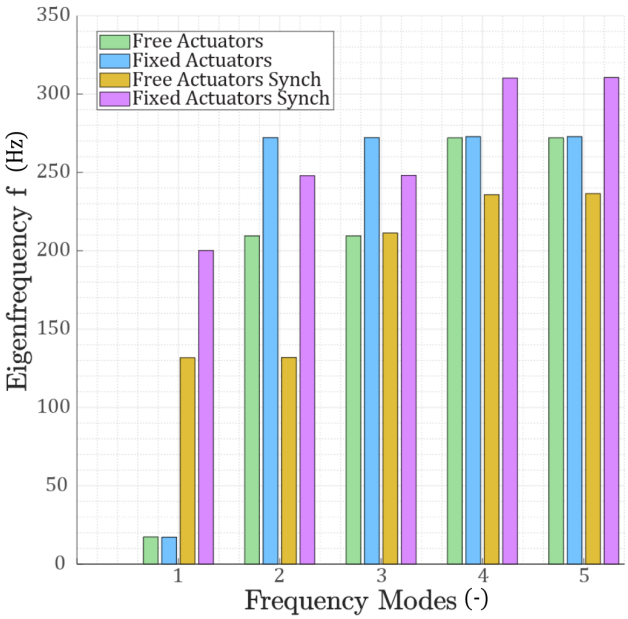

Fig. 26 Unwanted eigenfrequencies of the LAFP concept, with all frequencies being evaluated at the least favorable deflection. For a visual representation of the vibration modes, please consult Appendix E.

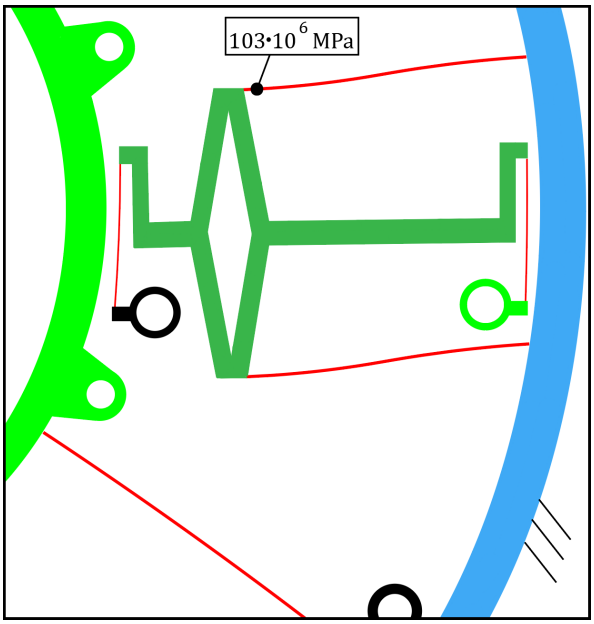

Fig. 27 Ansys simulation of the LAFP synchronizer in the deformed state. The maximum stress is located in the linear guide. Please note that the same color is used where parts are rigidly connected to each other.

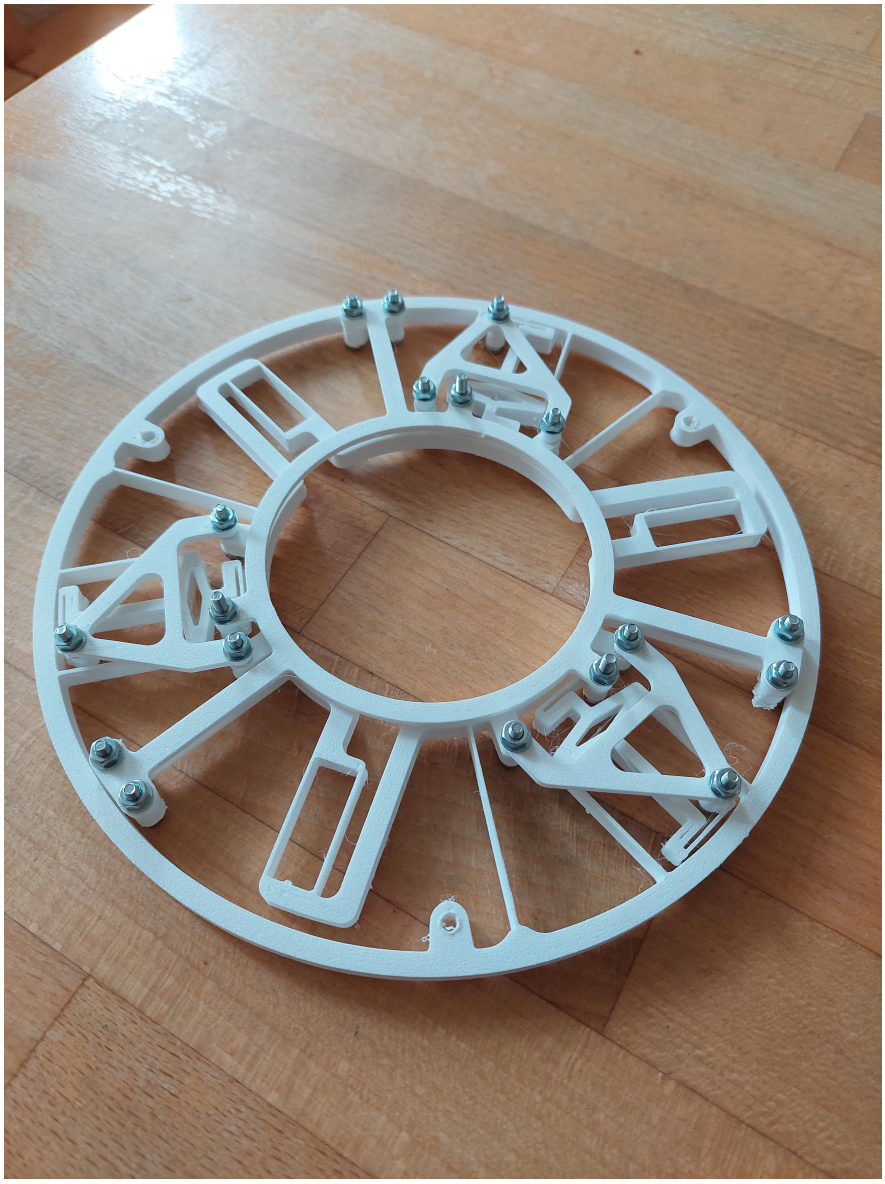

Fig. 28 3D-printed concept of the LAFP concept including the synchronizer using PLA-FDM.

6 Discussion

This research yields a mechanism that can be applied in an Atmospheric Dispersion Corrector as deployed in the Extremely Large Telescope. The requirement of the deflection angle is based on the observation times of the telescope and has been the source of much debate. While this work suggests a solution for the given deflection angle, a larger range of motion can be achieved by linking multiple designs in series. A new challenge will arise to improve the dynamic performance of such a device.

The analysis of the concepts showed that the introduction of compounding increases the performance such that a deflection angle of $\pm 4^{\circ}$ could be easily achieved. However, compounding also causes an unwanted Degree of Freedom that limits dynamic performance. The introduction of the linear guide to account for the shortening of the leaf springs (as seen in the LAFP and the TRIVOT concepts) increases the first unwanted eigenfrequency with a larger deflection angle. However, only purely parallel systems could achieve the first unwanted eigenfrequency of 70 Hz. While such a frequency can be improved by a synchronizer, the acceleration of approximately $3.5G$ as stated in the requirements must be countered by a locking mechanism that keeps the leaf springs from deflecting beyond the stress limit. The design of this mechanism is left as a recommendation.

The Large Angle Flexure Pivot and the Compounded Torsion Pivot are expanded upon with a dedicated synchronizer to eliminate these unwanted eigenfrequencies. While the design approach of the synchronizer for the LAFP is based on a design by Hopkins[26], it should be noted that a synchronizer design for both the CTP and the LAFP was not found in the literature. Optimizations of synchronizers to guarantee both optimal dynamic- and kinematic performance could be an upcoming and exciting research topic.

The CTP was computationally more expensive than the LAFP due to the load case of the design. Tapering was needed in order to optimize the stress levels in the leaf springs, and buckling analysis was needed due to the lateral load caused by the prism set. Furthermore, the CTP could only be optimized using *Ansys Workbench* because of the limitations of *SPACAR Light*. Future research into an alternative design of the CTP synchronizer using a linear guide similar to the LAFP is not done in this work, but could potentially improve performance.

Optimization of the LAFP was limited by computational times and the maximum number of nodes in *SPACAR Light*. To solve this issue, another version of this program was used which often drastically decreased simulation times. However, the accuracy of the results could not be trusted in this software version due to large differences with *SPACAR Light* and *Ansys*. It seems that future use of the new version is essential for the development of complex compliant mechanisms, especially when a synchronizer is included. Shorter simulation times could also cause possibilities using optimization algorithms that were not usable with the current version.

While both designs meet the requirements, the LAFP outperforms the CTP in terms of kinematic- and dynamical characteristics. Furthermore, the CTP only meets the requirements when the minimum thickness producible by Wire EDM is used, complicating the producability of the system. The impact of deviations

in flexure thickness using Wire EDM is not performed in this research. Moreover, the only material used is Aluminium 6061-T6 because of its well-known material properties in a cryogenic environment. Future research on flexure materials within a cryogenic environment would greatly increase the possibilities of the designer. Furthermore, the study of sintered metals in a cryogenic environment could open the doors to the use of Additive Manufacturing.

7 Conclusion

This research shows that a hollow single DoF compliant mechanism can be used to guide the optics of an Atmospheric Dispersion Corrector. The required deflection angle of $\pm 4^\circ$ is reached by using a variety of radially symmetric compounded concepts. It can be concluded that radially symmetric and purely parallel designs are unsuitable for this application due to limited deflection angles at the maximum actuation force. However, all concepts using a compounded configuration suffered from insufficient dynamical characteristics.

The only two concepts that had a single unwanted degree of freedom while meeting all kinematic requirements were the Compounded Torsion Pivot (CTP) and the Large Angle Flexure Pivot (LAFP). The compounded torsion pivot is analyzed to the effect of warping by including a tapered leaf spring design with an angle of 5.5°. The buckling factor because of lateral load caused by the prisms exceeds the minimum value of 10. While kinematic requirements are met, the CTP experiences a high slope stiffness reduction and stress increase with larger deflection angles. The LAFP is less complex to optimize due to the monolithic nature of the design. The introduction of the linear guides found in the LAFP increases the first unwanted eigenfrequency with increasing deflection. Both concepts were expanded with a synchronizer design, attempting to guide the motion of the intermediate body.

The CTP synchronizer consists of a lever and five flexure pivots. Both the intermediate body and the actuation stage are attached to the lever, forcing the intermediate body to move approximately half the distance of the actuation stage. While the synchronizer increases the unwanted eigenfrequency to 138.3 Hz, kinematic characteristics are greatly reduced. Moreover, the system only has enough deflection when the leaf spring width is diminished to the minimum value possible using Wire EDM.

The synchronizer of the LAFP utilizes a linear guide to force the actuation body to move the same amount as the intermediate body. However, as the intermediate body is found twice as far away from the pivot point, the relative motion of this body is halved. This synchronizer increases the first unwanted eigenfrequency while having a limited effect on kinematic characteristics. The leaf spring width of the mechanism is 0.3 mm for the main leaf springs, 0.24 mm for the linear guide, and 0.22 mm for the synchronizer.

Thus, it can be concluded that the synchronized adaptation of the Large Angle Flexure Pivot is the most suitable design for use in an Atmospheric Dispersion Corrector. The prism pair can be guided $\pm 4^\circ$ with a maximum leaf spring stress of 103 MPa, a lateral stiffness of $5.9 \cdot 10^6$ N/m, and a lowest unwanted eigenfrequency of 131.74 Hz.

Notes and references

1 Shorya Awtar. Synthesis and analysis of parallel kinematic xy flexure mechanisms. 2003.

2 Douglass L. Blanding. Machine design using kinematic processing, 1999.

3 Dannis Michel Brouwer, B.R. de Jong, and Herman Soemers. Mems based 6 degrees-of-freedom parallel kinematic precision micro manipulator. 2006.

4 D.M. Brouwer, J.P. Meijaard, and J.B. Jonker. Large deflection stiffness analysis of parallel prismatic leaf-spring flexures. *Precision Engineering*, 37(3):505–521, 2013.

5 Flavio Campanile and Alexander Hasse. A simple and effective solution of the elastica problem. *Proceedings of The Institution of Mechanical Engineers Part C-journal of Mechanical Engineering Science - PROC INST MECH ENG C-J MECH E*, 222:2513–2516, 12 2008.

6 Jorge Correa, Bonjin Koo, and Placid Ferreira. Parallel-kinematics xyz mems part 1: Kinematics and design for fabrication. *Precision Engineering*, 46:135–146, 2016.

7 Florent Cosandier, Philippe Schwab, Lionel Kiener, Johan Kruis, Laurent Giriens, Peter Spanoudakis, Christos Vrettos, and Georgia Psoni. Large angle flexure pivot development for high accuracy positioning of optical payloads. 06 2019.

8 Nicholas Dagalakis and Edward Amatucci. Kinematic modeling of a 6 degree of freedom tri-stage micro-positioner. 01 2001.

9 K. Gunnink, Ronald Aarts, and Dannis Michel Brouwer. Performance optimization of large stroke flexure hinges for high stiffness and eigenfrequency. 2013.

10 Layton Hale. Principles and techniques for designing precision machines. 01 1999.

11 Simon Henein, Peter Spanoudakis, Serge Droz, Leif Myklebust, and Emmanuel Onillon. Flexure pivot for aerospace mechanisms. *European Space Agency, (Special Publication) ESA SP*, 01 2003.

12 Jonathan B. Hopkins and Martin L. Culpepper. Synthesis of multi-degree of freedom, parallel flexure system concepts via freedom and constraint topology (fact) – part i: Principles. *Precision Engineering*, 34(2):259–270, 2010.

13 Larry L. Howell. Compliant mechanisms, 2001.

14 Yong Huang and Qi-Zhi Luo. A simple method to determine the critical buckling loads for axially inhomogeneous beams with elastic restraint. *Computers Mathematics with Applications*, 61(9):2510–2517, 2011.

15 J. B. Jonker and J. P. Meijaard. *SPACAR — Computer Program for Dynamic Analysis of Flexible Spatial Mechanisms and Manipulators*, pages 123–143. Springer Berlin Heidelberg, Berlin, Heidelberg, 1990.

16 Dongwoo Kang and Daegab Gweon. Analysis and design of a cartwheel-type flexure hinge. *Precision Engineering*, 37(1):33–43, 2013.

17 P. C. Kohnke. *ANSYS*, pages 19–25. Springer Berlin Heidelberg, Berlin, Heidelberg, 1982.

18 Helge Kragh. The lorenz-lorentz formula: Origin and early history. 2018.

19 Mingxiang Ling, Junyi Cao, Larry L. Howell, and Minghua Zeng. Kinetostatic modeling of complex compliant mechanisms with serial-parallel substructures: A semi-analytical matrix displacement method. *Mechanism and Machine Theory*, 125:169–184, 2018.

20 Qibo Mao. Free vibration analysis of multiple-stepped beams by using adomian decomposition method. *Mathematical and Computer Modelling*, 54(1):756–764, 2011.

21 Patrick Merken, Olivier Smal, Jean-François

Debongnie, and Benoit Raucent. Mechanical based circular notch hinge design. 01 2007.

22 M. Naves, D. M. Brouwer, and R. G. K. M. Aarts. Building Block-Based Spatial Topology Synthesis Method for Large-Stroke Flexure Hinges. *Journal of Mechanisms and Robotics*, 9(4):041006, 05 2017.

23 Mark Naves, Marijn Nijenhuis, W.B.J. Hakvoort, and D.M. Brouwer. Flexure-based 60 degrees stroke actuator suspension for a high torque iron core motor. *Precision Engineering*, 63, 02 2020.

24 Mark Naves, Marijn Nijenhuis, Bram Seinhorst, Wouter Hakvoort, and Dannis M. Brouwer. T-flex: A fully flexure-based large range of motion precision hexapod. *Precision engineering*, 72:912–928, November 2021.

25 M. Nijenhuis, J.P. Meijaard, and D.M. Brouwer. Misalignments in an overconstrained flexure mechanism: A cross-hinge stiffness investigation. *Precision Engineering*, 62:181–195, 2020.

26 Robert M. Panas and Jonathan B. Hopkins. Eliminating Underconstraint in Double Parallelogram Flexure Mechanisms. *Journal of Mechanical Design*, 137(9):092301, 07 2015.

27 Robert M. Panas, Frederick Sun, Logan Bekker, and Jonathan B. Hopkins. Combining cross-pivot flexures to generate improved kinematically equivalent flexure systems. *Precision Engineering*, 72:237–249, 2021.

28 Jerome M. Paros. How to design flexure hinges. 1965.

29 Xu Pei, Jingjun Yu, Guanghua Zong, Shusheng Bi, and Haijun Su. The modeling of cartwheel flexural hinges. *Mechanism and Machine Theory*, 44(10):1900–1909, 2009.

30 A. Picard and H. Fang. Comparison of three methods to determine the density of moist air. pages 314–315, 2002.

31 A. R. Smith, S. Gwo, and C. K. Shih. A new high-resolution two-dimensional micropositioning device for scanning probe microscopy applications. *Review of Scientific Instruments*, 65(10):3216–3219, 10 1994.

32 Peter Spanoudakis, Lionel Kiener, Florent Cosandier, Philippe Schwab, Laurent Giriens, Johan Kruis, Daniel Grivon, Georgia Psoni, Christos Vrettos, and Nabil Bencheikh. Large angle flexure pivot development for future science payloads for space applications. *MATEC Web of Conferences*, 304:07016, 01 2019.

33 Etienne Thalmann, Quentin Gubler, and Simon Henein. Gravity-compensation design approaches for flexure-pivot time bases. *Machines*, 10(7), 2022.

34 J. A. van den Born, R. Romp, A. W. Janssen, R. Navarro, W. Jellema, E. Tolstoy, B. Jayawardhana, and M. Hartl. The micado atmospheric dispersion corrector: Optomechanical design, expected performance and calibration techniques, 2022.

35 J A van den Born and W Jellema. Quantification of the expected residual dispersion of the MICADO Near-IR imaging instrument. *Monthly Notices of the Royal Astronomical Society*, 496(4):4266–4275, 06 2020.

36 Bachar Wehbe, Alexandre Cabral, Jorge Martins, P. Figueira, Nuno Santos, and Gerardo Ávila. The impact of atmospheric dispersion in the performance of high-resolution spectrographs. 11 2019.

37 Jianwei Wu, Shuai Cai, Jiwen Cui, and Jiubin Tan. A generalized analytical compliance model for cartwheel flexure hinges. *Review of Scientific Instruments*, 86:105003, 10 2015.

38 Andrew T. Young. Sunset science. iv. low-altitude refraction. *The Astronomical Jour-*

nal, 127(6):3622, jun 2004.

39 Yue-Qing Yu, Qian Li, and Qiping Xu. Pseudo-rigid-body dynamic modeling and analysis of compliant mechanisms. *Proceedings of the Institution of Mechanical Engineers, Part C: Journal of Mechanical Engineering Science*, 232:095440621770754, 05 2017.

40 Aimei Zhang and Guimin Chen. A Comprehensive Elliptic Integral Solution to the Large Deflection Problems of Thin Beams in Compliant Mechanisms. *Journal of Mechanisms and Robotics*, 5(2), 03 2013.

Appendix A: The ELT, MICADO, and the ADC

This appendix expands upon the background information given about the ELT, the MICADO near-infrared instrument, and the ADC.

The ELT

On the eleventh of December, 2006, the ESO council decided to proceed with detailed studies for the ELT. The telescope is expected to see its first light in 2028. Science cases include

- Solar System Research - Volcanic activity and the watery plumes on the moons of Jupiter and Saturn will be studied, along with the origin of asteroids and comets. Due to the large sensitivity of the telescope, the faintest objects in the Solar System can be studied. The ELT can also be used to gain a better insight into the creation and evolution of the Solar System by studying the objects in the Asteroid Belt between Mars and Jupiter and the Kuiper Belt beyond Neptune.

- Exoplanets - The ELT will provide new insights into planets outside our Solar System. It will be able to obtain images of planets in the habitable zones of a star. Due to the very large collecting power of the ELT, transiting planets' atmospheres can be studied as they pass in front of their parent star.

- Stars - With the new capabilities of the ELT, the formation of stars can be studied with ten times the detail that is possible today. Astronomers will also be able to look beyond our Galactic neighborhood to look into individual stars in distant galaxies.

- Black Holes - The center of the Milky Way can be examined in more detail for exploring gravity around the closest supermassive black hole. A dense cluster of stars surrounds the supermassive black hole and can be studied for their behavior in their environment. Supermassive black holes can also be characterized out to large distances with the ELT, which enables the search for the formation of supermassive central objects.

- Galaxies - The ELT will be able to observe red-shifted galaxies, giving insight into the perception of the Universe. The ELT can also look into individual stars in distant galaxies, and study the interplay between galaxies and the surrounding intergalactic medium which serves as a reservoir of gas for the ongoing infall of fresh material in galaxies.

- Cosmology and Dark Matter - The ELT can assist in the model of General Relativity to explain the expansion of the Universe, including testing gravity in the most unexplored places and mapping the expansion itself.

- Fundamental Physics - Fundamental constants of nature are assumed to be constant in the entire universe. However, if this assumption does not hold, a different location and epoch may change these constants. The ELT will assist in the ongoing searches for possible variations in fundamental physical constants across space and time.

NOVA is a collaboration of four Dutch Universities that together define the Dutch Astronomical agenda. NOVA-ASTRON, located in Dwingeloo and hosted by ASTRON, is its Optical and Infrared Instrumentation Group which develops, produces, and tests the next generation of astronomical instruments. It is specialized in the design and production of precision mechanisms and cryogenic systems. Currently, the main focus of NOVA is on developing the instruments for the Extremely Large Telescope (ELT), in particular, MICADO which is a Multi-AO Imaging Camera for Deep Observations, and METIS which is The Mid-Infrared E-ELT Imager and Spectrograph. The focus of this research is a mechanism within MICADO, where a light beam entering the cryostat will be collimated, filtered depending on the wavelength requirements of the experiment, and passed through one of the four sets of optical components. Before the light enters the main selection mechanism, an Atmospheric Dispersion Corrector is used.

Atmospheric Dispersion Correction

One of the most difficult challenges for high-resolution images of the universe from ground telescopes is the atmosphere. At large distances from Zenith, Atmospheric Dispersion (or wavelength-dependent refraction) causes significant challenges in imaging. The atmosphere acts like a prism, dispersing blue light more than red light. If a planet exhibits atmospheric dispersion effects, the image will have a blue fringe on the top edge and a red fringe on the bottom edge. The larger the angle of the light while meeting the atmosphere, the more the light is dispersed into blue and red parts 1. However, while observing normal to the Earth's surface, no dispersion is present and no correction is needed. As presented in the main text, the ADC consists of two sets of optical prisms, which can rotate against each other. Using this rotation, the light is reconverged, causing the opposite dispersion and refracting the light back to the focal point on the detector.

The current conventionally designed ADC mechanism is a gearless friction drive that serves as a suspension at the same time (figure 29). This is advantageous for temperature-induced shrinkage differences. The actuator can be switched off when the prisms do not have to rotate, reducing thermal load. The backlash of the friction drive is sufficiently small. In a cryogenic environment, the only way to thermally heat the prisms is through radiation. This is a frictionless solution but requires a large radiation surface. The preload of the friction wheels is calculated such that the force from the rotating mass due to radial acceleration will not exceed the preload force.
A prototype was made of the design, and tested in detail. From the experiments, it was evident that the accuracy requirements were only just met. In terms of accuracy, the requirements are met. However, using a powerful motor and going through the wear on the wheel and rollers is not a lasting solution. If the contact point between the roller and the mechanism would be extremely small, this would not be an issue. However, in practice, the contact point is larger than anticipated.

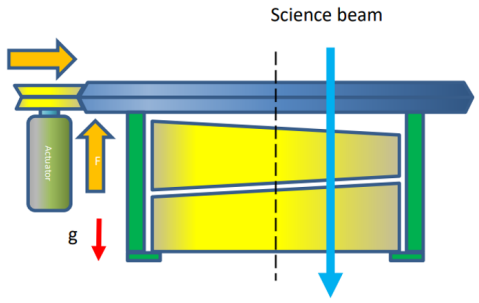

Fig. 29 Current design of the ADC-mechanism developed by NOVA. (Source: Test report of NOVA)

Requirement analysis for the ADC

Due to the high wear of the ADC friction wheels, the objective is to reduce the time that they must rotate by introducing a secondary mechanism. The friction wheels will turn the prisms to their correct initial position, locking them in place. Then, a compliant mechanism will rotate the prisms to exactly counter the atmospheric dispersion. This will not only reduce the operating time of the friction wheels but will also increase the position accuracy. Relations between the Zenith angle and the Rotation angle, as well as the Zenith angle and the Residual Dispersion, are given in figure 34.

The equation for the optimal position of the ADC top prism pair is then calculated with

$$\theta_1 = \cos^{-1}\left(c_f \tan(z)\right) \tag{15}$$

and

$$c_f = \frac{D_{EPD}}{D_{ADC}} \frac{\Delta n_{atm}}{\Delta n_{S-LAH71}(A_1 + A_4) + \Delta n_{S-FPL51}(A_2 + A_3)} \tag{16}$$

where θ_1 is the ideal rotation angle of the ADC top prism pair. For the bottom pair, we say that $\theta_2 = -\theta_1$. Such that the ADC is in the neutral position when the dispersion angle is zero. Furthermore, we have that

- c_f Filter- and atmosphere- dependent
- z Zenith angle (zero straight up)
- D_{EPD} 35.542 meters, the diameter of the ELT Mirror 1
- D_{ADC} 0.079 meter, footprint at the ADC
- $\Delta n_{S-LAH71}$ Filter dependent variable
- $A_1 = A_4$ 4.63387°, Apex angle of the prisms
- $A_2 = A_3$ -7.77233°, Apex angle of the prisms
- $\Delta n_{S-FPL51}$ Filter dependent variable
- Δn_{atm} Atmosphere dependent variable

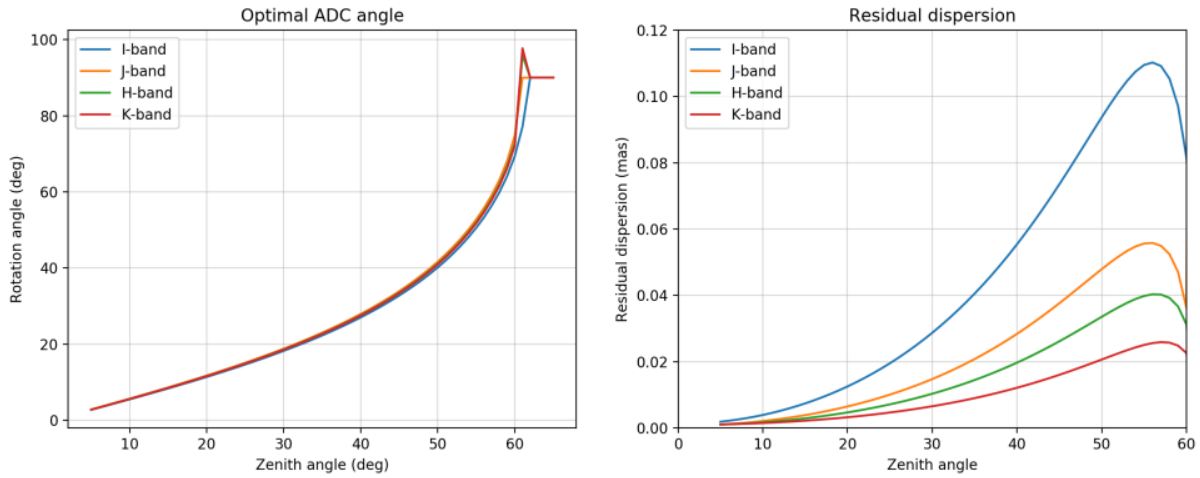

Fig. 30 Left: Optimal rotation angle of the prisms relative to the Zenith angle of the telescope. Right: Residual dispersion relative to the Zenith angle. (Source: Test report of NOVA)

Of course, the dispersion vector of the ADC should be opposite to the atmospheric dispersion vector, which is why the field rotation is also brought into consideration, with

$$\theta_{p1} = \theta_1 + \theta_{FR} \tag{17}$$

$$\theta_{p2} = -\theta_1 + \theta_{FR} \tag{18}$$

This field rotation θ_{FR} is large at near-Zenith, where the atmospheric dispersion present is small. This concludes the analysis of the position of the prisms. Next, the velocity and acceleration requirements are stated. For the second stage, the current velocity requirements are used. The flexure mechanism must be able to rotate the prisms a total of 8 degrees within a maximum time of 120 seconds. For acceleration limits, it is stated that the maximum g-forces on the mechanism can be $2.6g$ radially and $1.9g + 1g$ static axially. This is the result of a risk analysis of the severity of earthquakes in the area where the telescope is built.

Appendix B: Existing 1 DoF rotational compliant mechanisms

In this appendix, numerous existing compliant mechanisms are presented including their respective advantages and disadvantages. The abundance of possible geometries is greatly restricted by the need for the optical aperture in the center of the compliant mechanism.

Image	Title	Advantages	Disadvantages
	Leaf spring	• Manufacturability • Well understood • High deflection range • Symmetric design	• Reduced precision at large deflection ranges due to center shift caused by parasitic motion • Low lateral support stiffness • Central geometry essential
[21] 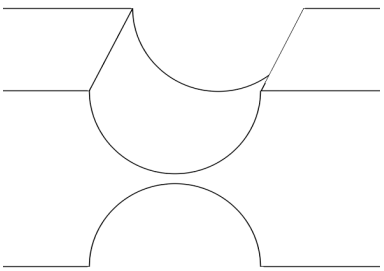	Notch Hinge	• Manufacturability • High lateral support stiffness[21] • Easy to miniaturize • Symmetric design	• Low deflection angles • High stress concentration[21] • Central geometry essential
[37] 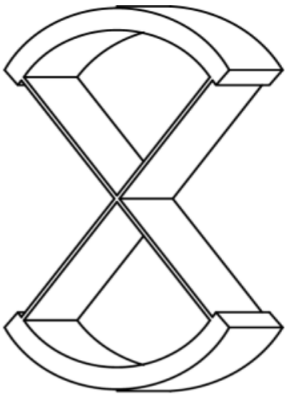	Cartwheel Hinge	• Can be expanded with an optical aperture • High lateral support stiffness[37] • Symmetric design • Can be radially symmetric when the optical aperture is introduced	• High stress concentration in the center[37] • Reduced precision at large deflection ranges due to center shift caused by parasitic motion

Table 3 First three concepts

Image	Title	Advantages	Disadvantages
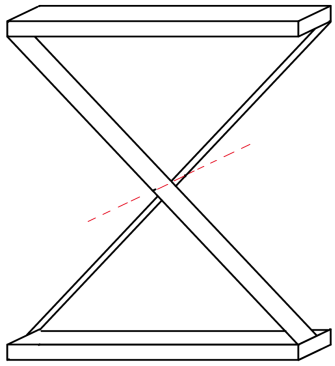	Flexure Pivot	• Relatively high deflection range • Low stress • High support stiffness[27]	• Not monolithic, must be either assembled or 3D-printed. • Not symmetric • Warping can occur at large deflection angles[27]
29 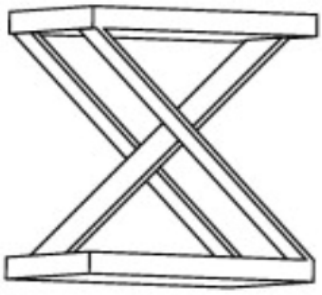	Symmetrical cross hinge	• Relatively high deflection range • Low stress[29] • Symmetric design	• Can only be made using assembly or 3D-printing • Reduced precision at large deflection ranges due to center shift caused by parasitic motion[29] • Central geometry essential
24 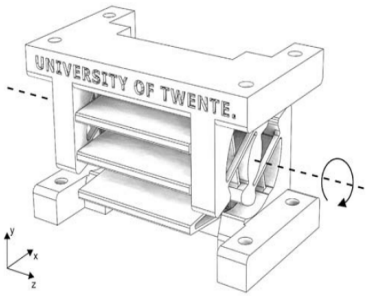	T-flex	• Large deflection angle • Can be optimized to have eight times the support stiffness of the symmetrical cross-hinge[24] • Can be optimized to have high parasitic eigenfrequencies[24]	• Difficult to manufacture (Produced with 3D-printing) • Central geometry essential

Table 4 Concepts 4-7

Image	Title	Advantages	Disadvantages
9 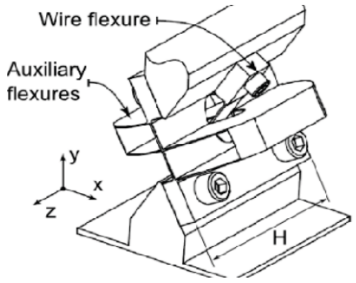	Infinity Hinge	• Large deflection angle • Optimized for high lateral support stiffness • High unwanted eigenfrequencies[9] • Does not have to be 3D-printed	• The wire flexure makes the design non-monolithic • Not symmetric[9] • Geometry in the center is essential
33 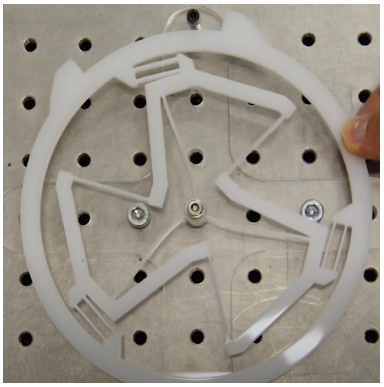	TRIVOT-flexure	• Large deflection angle made possible by the introduced linear guides • Fully monolithic (extrudable) design[33] • Radially symmetric (no center shift) • Can be expanded with an optical aperture	• Linear guides limit the length of the major leaf springs[33] • Optical aperture limits the length of the major leaf springs • Serial design, unwanted degrees of freedom can be present[33]
33 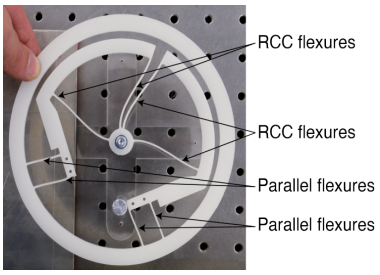	ROC-flexure	• Can be expanded with an optical aperture • Fully monolithic (extrudable) design[33] • Axially symmetric • Large deflection angle made possible by the introduced linear guides	• Serial design, unwanted degrees of freedom can be present • Not radially symmetric

Table 5 Concepts 8-11

Image	Title	Advantages	Disadvantages
7 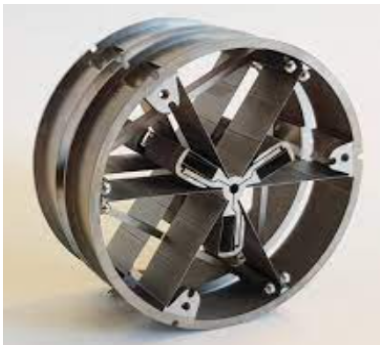	Large Angle Flexure Pivot	• (Very) high deflection range[7] • Linear guides do not limit the main leaf spring length • Radially symmetric • Can be expanded with an optical aperture	• Complex to manufacture • Optical aperture limits the main leaf spring length • Serial design, unwanted Degrees of Freedom may occur[7]
10 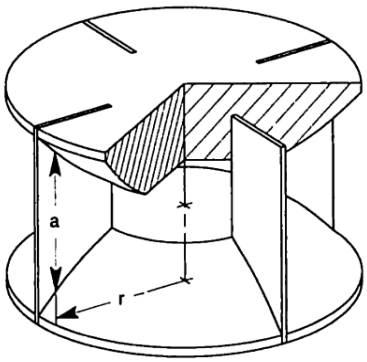	Torsion Pivot	• Can be expanded with an optical aperture • Optical aperture does not limit the main leaf spring length • High support stiffness for small deformations[10] • Radially symmetric	• Complex to manufacture • Limited deflection angle • Complex stress profile due to the effect of warping[10] • Leaf spring length limited by building height

Table 6 Concepts 12 and 13

Appendix C: Ansys and *Solidworks* guide

This Appendix serves as a visual guide for the workflow between *SolidWorks* and *Ansys*. The author of this work found that a guide for this type of research is exceedingly difficult to find. This guide may help future students investigate compliant mechanisms using *Ansys*.

Step 1: Develop *SolidWorks* model and save as *.Parasolid*

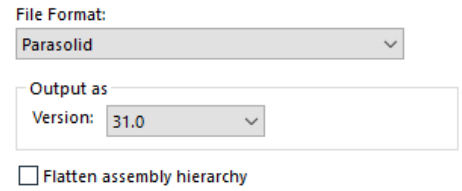

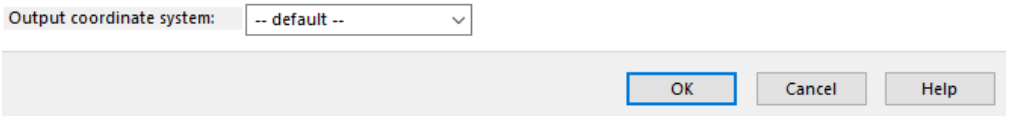

Step 2: Open *Ansys Workbench*. Select the required engineering data, and import the *.Parasolid* into *Spaceclaim* in either a Static Structural or Modal Analysis.

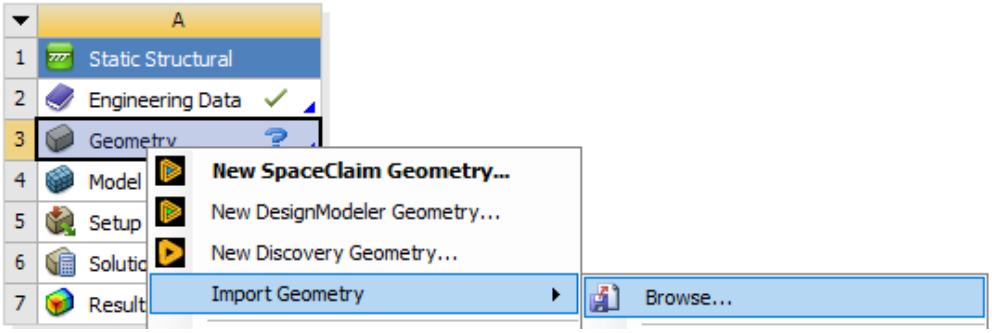

Step 3: Open Spaceclaim. In the design tab, select *split body*. Select the model and *local slicing*, then cut the leaf spring from the rest of the geometry as shown below.

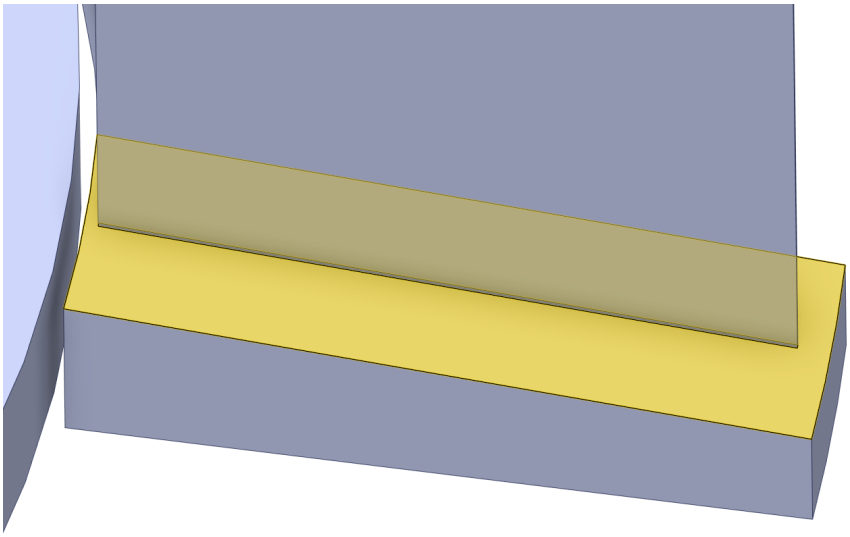

Step 4: Once all the leaf springs are cut as a separate body, select the entire model and use the *share* feature. The model is now considered one body, but meshing can be applied on the leaf springs separately.

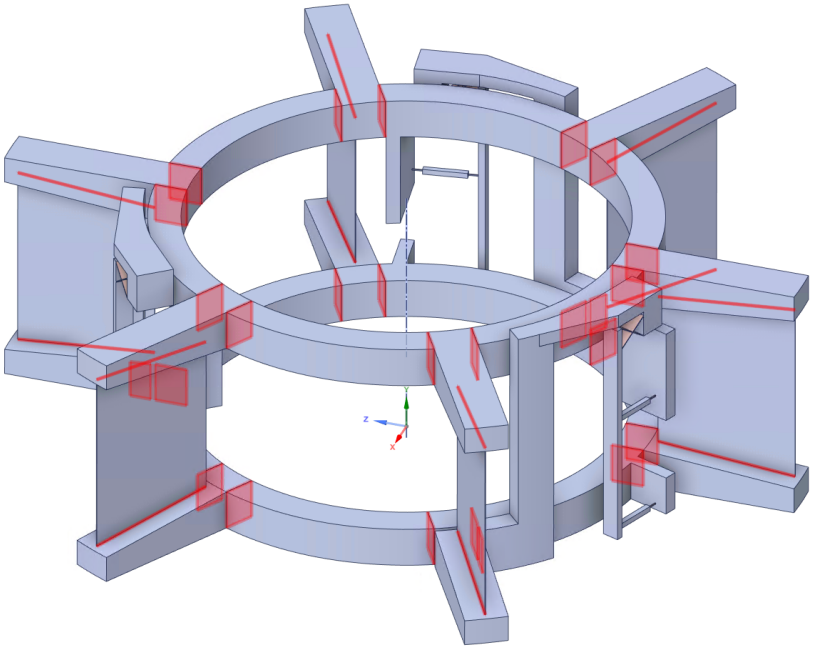

Step 5: Edit the model in *Ansys Workbench*. Select the proper material, and add the mass of the payload including the inertia obtained from *SolidWorks* with *mass properties*.

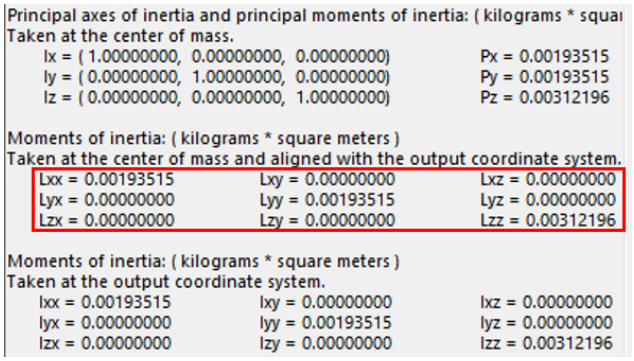

Principal axes of inertia and principal moments of inertia: (kilograms * squa
Taken at the center of mass.

Ix = (1.00000000,	0.00000000,	0.00000000)
Iy = (0.00000000,	1.00000000,	0.00000000)
Iz = (0.00000000,	0.00000000,	1.00000000)

Px = 0.00193515		
Py = 0.00193515		
Pz = 0.00312196		

Moments of inertia: (kilograms * square meters)
Taken at the center of mass and aligned with the output coordinate system.

Lxx = 0.00193515	Lxy = 0.00000000	Lxz = 0.00000000
Lyx = 0.00000000	Lyy = 0.00193515	Lyz = 0.00000000
Lzx = 0.00000000	Lzy = 0.00000000	Lzz = 0.00312196

Moments of inertia: (kilograms * square meters)
Taken at the output coordinate system.

Ixx = 0.00193515	Ixy = 0.00000000	Ixz = 0.00000000
Iyx = 0.00000000	Iyy = 0.00193515	Iyz = 0.00000000
Izx = 0.00000000	Izy = 0.00000000	Izz = 0.00312196

Step 6: In *Workbench*, select each leaf spring and add a *method*, and *mesh sizing* for all leaf springs. The detail of the mesh depends on the user case. In the general mesh settings, make sure there is no mesh defeaturing. Generate the mesh.

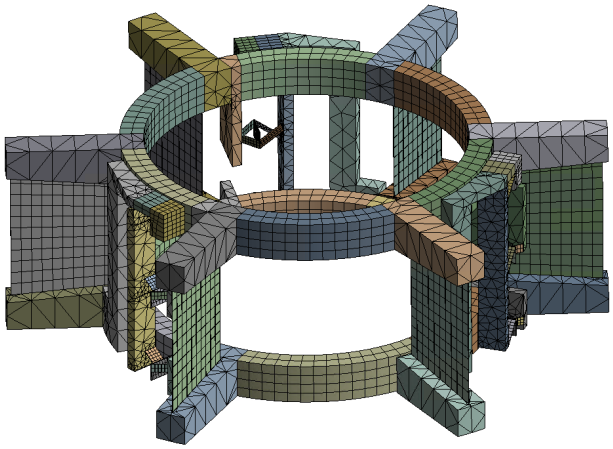

Step 7: Add the constraints and loads like any other *Ansys* analysis. To read out the deflection angle θ of the compliant mechanism, add in a *Remote Point* anywhere on the actuation stage. Give this point the command $x = npilot$. In the results tab, write a command $\theta = ROTZ(z) * \frac{180}{\pi}$.

Step 8: Select *Large Deflections* in the *Analysis* tab. If not, the solution to the problem will not be accurate when analyzing compliant mechanisms! After this, the setup can be simulated.

Appendix D: Limits of Spacarlight

The software *SPACAR Light* is a great tool for analyzing compliant mechanisms with a limited number of flexible elements. Each flexible element consists of several beams, each considered to be flexible with six deformation modes. When the model expands to about 90 nodes and 110 elements, an error is given regarding a license problem. This is however an error that has to do with the limits of what can be done within the software *SPACAR Light*.

Spacar "1.5"

Another version of the software was developed by Dr. Ir. M. Nijenhuis, allowing for larger models to be analyzed as well. However, testing with the software yielded large differences between *SPACAR Light*, *Ansys*, and *Spacar* 1.5. The deviation of the solution increased with model complexity. One of the developed models is displayed below. While the software was not usable for these reasons, experimentation showed that *Spacar* 1.5 was up to 14 times faster than *SPACAR Light*. Therefore, further development of this updated version will greatly benefit any future research on complex compliant mechanisms.

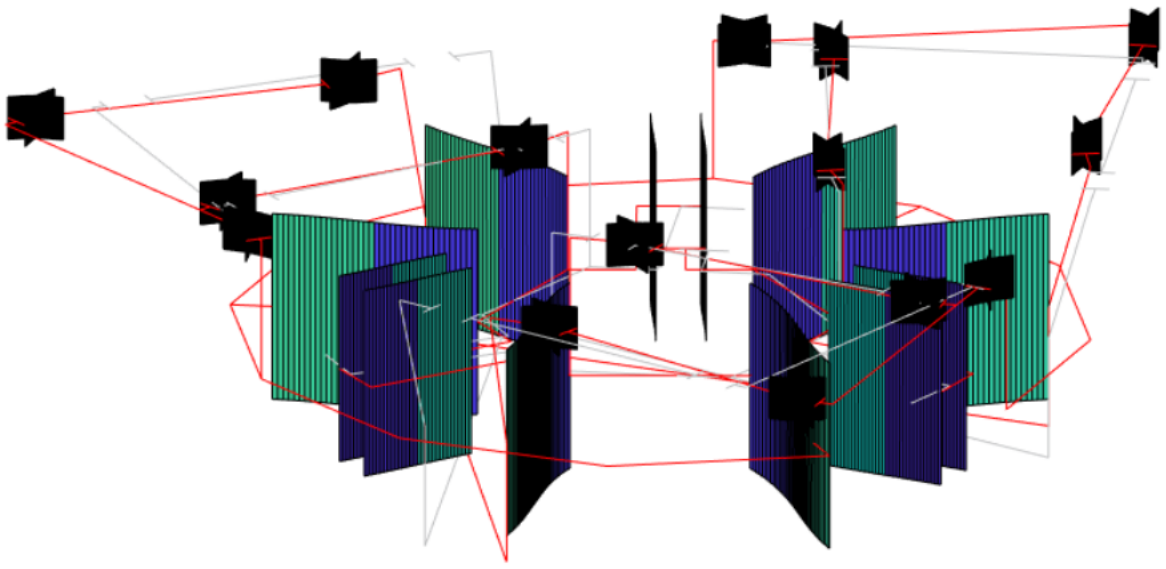

Fig. 31 Complex models in Spacar 1.5

Appendix E: LAFP modes

This appendix includes a close-up of the synchronizer movement in the different vibration modes. Then, the intended motion of the LAFP including the synchronizer is displayed

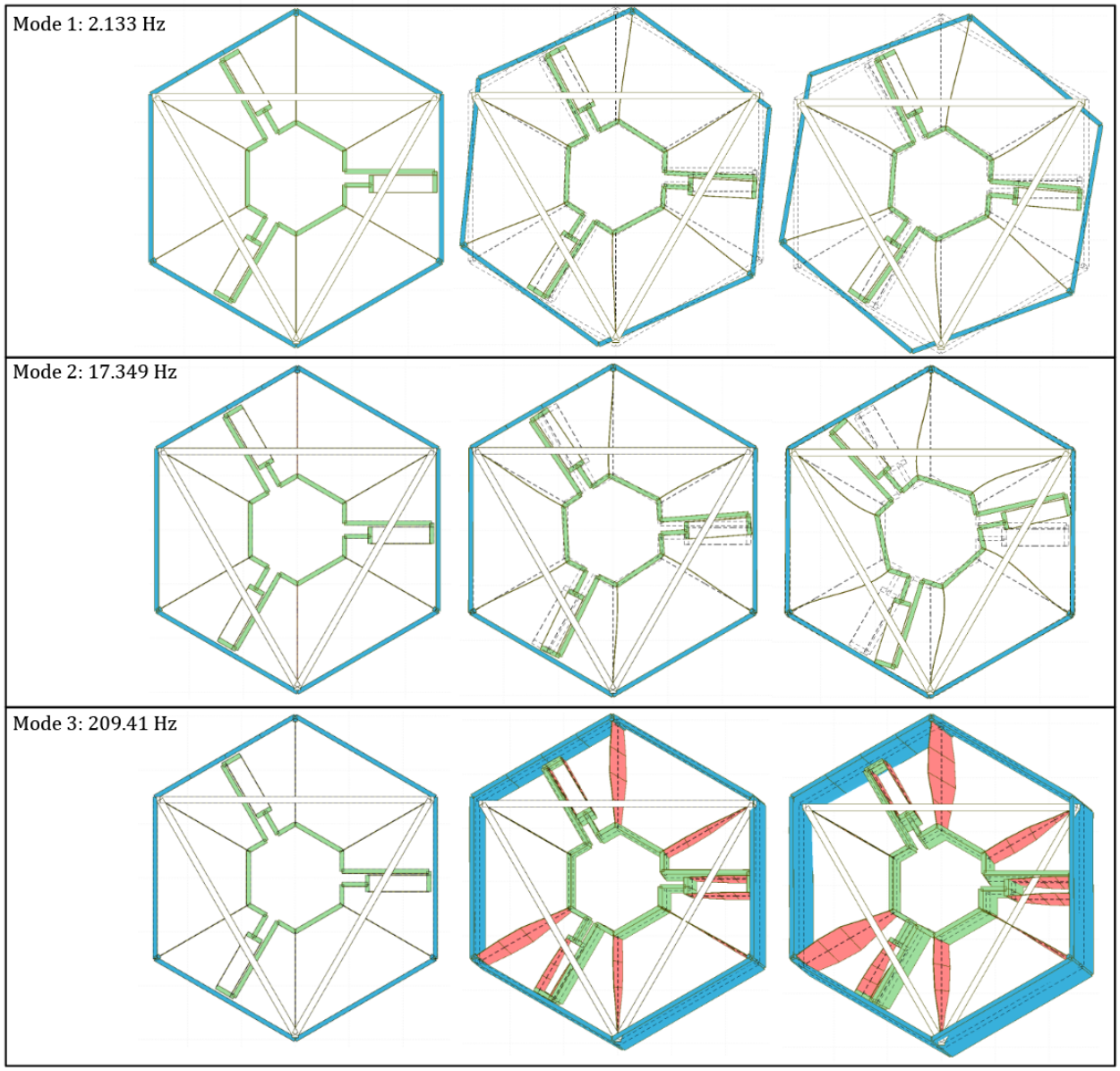

Fig. 32 LAFP vibration modes without synchronizer

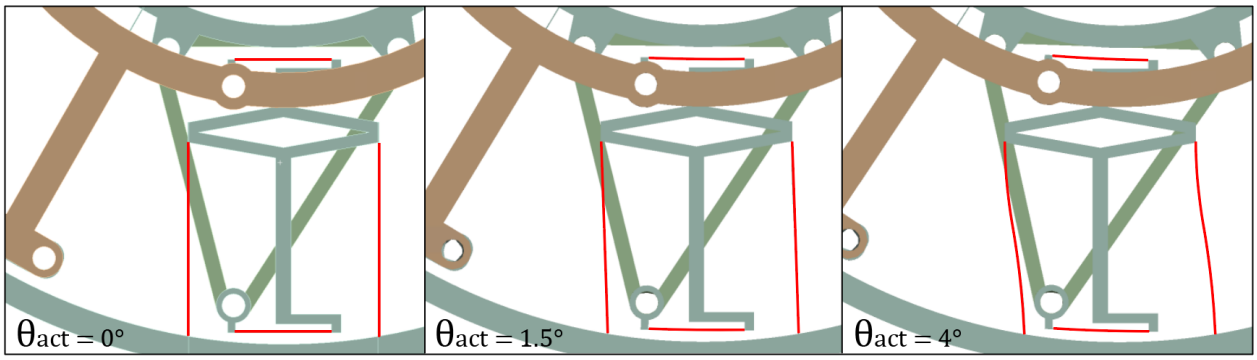

Fig. 33 Elimination of the second vibration mode through a synchronizer utilizing a linear guide.

Appendix F: LAFP Spacarlight Code

In this Appendix, the coordinate equations of the LAFP are given as it is used in *SPACAR Light* (without the synchronizer). Displaying the entire code is omitted for readability reasons.

$$(1) = [0, \frac{1}{2} * Gap, 0] \tag{19}$$

$$(2) = [\frac{1}{2} * Gap * cos(30), \frac{1}{2} * Gap * sin(30), 0] \tag{20}$$

$$(3) = [\frac{1}{2} * Gap * cos(30), \frac{1}{2} * Gap * tan(G_d) * cos(30), 0] \tag{21}$$

$$(4) = [\frac{1}{2} * Gap * cos(30) + L_{lin} + L_r, \frac{1}{2} * Gap * tan(G_d) * cos(30), 0] \tag{22}$$

$$(5) = [\frac{1}{2} * Gap * cos(30) + L_{lin} + L_r, \frac{1}{2} * Gap * tan(G_d) * cos(30) - L_{r3}, 0] \tag{23}$$

$$(6) = [\frac{1}{2} * Gap * cos(30) + L_{lin} + L_r, \frac{1}{2} * Gap * tan(G_d) * cos(30) - L_{r2}, 0] \tag{24}$$

$$(7) = [\frac{1}{2} * Gap * cos(30) + L_r, \frac{1}{2} * Gap * tan(G_d) * cos(30) - L_{r2}, 0] \tag{25}$$

$$(8) = [\frac{1}{2} * Gap * cos(30) + L_r, -\frac{1}{2} * Gap * tan(G_d) * cos(30) - L_{r3}, 0] \tag{26}$$

$$(9) = [\frac{1}{2} * Gap * cos(30) + L_r, -\frac{1}{2} * Gap * tan(G_d) * cos(30), 0] \tag{27}$$

$$(10) = [\frac{1}{2} * Gap * cos(30), -\frac{1}{2} * Gap * tan(G_d) * cos(30), 0] \tag{28}$$

$$(11) = [\frac{1}{2} * Gap * cos(30), -\frac{1}{2} * Gap * sin(30), 0] \tag{29}$$

$$(12) = [0, -\frac{1}{2} * Gap, 0] \tag{30}$$

$$(13) = [-cos(30) * D_{rig}, -\frac{1}{2} * Gap + sin(30) * D_{rig}, 0] \tag{31}$$

$$(14) = [-cos(30) * D_{rig} - cos(60) * (L_{lin} + L_r), -\frac{1}{2} * Gap + sin(30) * D_{rig} - sin(60) * (L_{lin} + L_r), 0] \tag{32}$$

$$(15) = [-cos(30) * D_{rig} - cos(60) * (L_{lin} + L_r) - cos(30) * L_{r3}, -\frac{1}{2} * Gap + sin(30) * D_{rig} - sin(60) \tag{33}$$

$$* (L_{lin} + L_r) + sind(30) * L_{r3}, 0] \tag{34}$$

$$(16) = [pos_{15x} - cos(30) * (L_{r2} - L_{r3}), pos_{15y} + sind(30) * (L_{r2} - L_{r3}), 0] \tag{35}$$

$$(17) = [pos_{15x} - cos(30) * (L_{r2} - L_{r3}) + cos(60) * L_{lin}, pos_{15y} + sind(30) * (L_{r2} - L_{r3}) + sin(60) * L_{lin}, 0] \tag{36}$$

$$(18) = [pos_{15x} + cos(60) * L_{lin}, pos_{15y} + sin(60) * L_l in, 0] \tag{37}$$

$$(19) = [pos_{15x} + cos(60) * L_{lin} - cos(30) * L_{pos}, pos_{15y} + sin(60) * L_l in + sin(30) * L_{pos}, 0] \tag{38}$$

$$(20) = [pos_{15x} + cos(60) * L_{lin} - cos(30) * L_{pos} + cos(60) * L_r, pos_{15y} + sin(60) * L_l in + sin(30) * L_{pos} + \tag{39}$$

$$sin(60) * L_r, 0] \tag{40}$$

$$(21) = [-\frac{1}{2} * Gap * cos(30), -\frac{1}{2} * Gap * sin(30), 0] \tag{41}$$

$$(22) = [-\frac{1}{2} * Gap * cos(30), \frac{1}{2} * Gap * sin(30), 0] \tag{42}$$

$$(23) = [-\frac{1}{2} * Gap * cos(30) + D_{rig} * cos(30), \frac{1}{2} * Gap * sin(30) + D_{rig} * sin(30), 0] \tag{43}$$

$$(24) = [-\frac{1}{2} * Gap * cos(30) + D_{rig} * cos(30) - cos(60) * (L_{lin} + L_r), \frac{1}{2} * Gap * sin(30) + D_{rig} * sin(30) + \tag{44}$$

$$sin(60) * (L_{lin} + L_r), 0] \tag{45}$$

$$(25) = [-\frac{1}{2} * Gap * cos(30) + D_{rig} * cos(30) - cos(60) * (L_{lin} + L_r) + cos(30) * L_{r3}, \frac{1}{2} * Gap * sin(30) + \tag{46}$$

$$D_{rig} * sin(30) + sin(60) * (L_{lin} + L_r) + sin(30) * L_{r3}, 0] \tag{47}$$

$$(26) = [pos_{25x} + cos(30) * (L_{r2} - L_{r3}), pos_{25y} + sin(30) * (L_{r2} - L_{r3}), 0] \tag{48}$$

$$(27) = [pos_{25x} + cos(30) * (L_{r2} - L_{r3}) + cos(60) * L_{lin}, pos_{25y} + sin(30) * (L_{r2} - L_{r3}) + sin(60) * L_{lin}, 0] \tag{49}$$

$$(28) = [pos_{25x} + cos(60) * L_{lin}, pos_{25y} + sin(60) * L_{lin}, 0] \tag{50}$$

$$(29) = [pos_{25x} + cos(60) * L_{lin} + cos(30) * L_{pos}, pos_{25y} + sin(60) * L_{lin} + sin(30) * L_{pos}, 0] \tag{51}$$

$$(30) = [pos_{25x} + cos(60) * L_{lin} + cos(30) * L_{pos} + cos(60) * L_r, pos_{25y} + sin(60) * L_{lin} + sin(30) * L_{pos} + \tag{52}$$

$$sin(60) * L_r, 0] \tag{53}$$

$$(31) = [0, \frac{1}{2} * Gap + L_{flex}, 0] \tag{54}$$

$$(32) = [cos(30) * (\frac{1}{2} * Gap + L_{flex}) sin(30) * (\frac{1}{2} * Gap + L_{flex}), 0] \tag{55}$$

$$(33) = [cos(60) * (\frac{1}{2} * Gap + L_{flex}) sin(60) * (\frac{1}{2} * Gap + L_{flex}), 0] \tag{56}$$

$$(34) = [cos(90) * (\frac{1}{2} * Gap + L_{flex}) sin(90) * (\frac{1}{2} * Gap + L_{flex}), 0] \tag{57}$$

$$(35) = [cosn(120) * (\frac{1}{2} * Gap + L_{flex}) sin(120) * (\frac{1}{2} * Gap + L_{flex}), 0] \tag{58}$$

$$(36) = [cos(150) * (\frac{1}{2} * Gap + L_{flex}) sin(150) * (\frac{1}{2} * Gap + L_{flex}), 0] \tag{59}$$

$$(37) = [cos(180) * (\frac{1}{2} * Gap + L_{flex}) sin(180) * (\frac{1}{2} * Gap + L_{flex}), 0] \tag{60}$$

$$(38) = [cos(210) * (\frac{1}{2} * Gap + L_{flex}) sin(210) * (\frac{1}{2} * Gap + L_{flex}), 0] \tag{61}$$

$$(39) = [cos(240) * (\frac{1}{2} * Gap + L_{flex}) sin(240) * (\frac{1}{2} * Gap + L_{flex}), 0] \tag{62}$$

$$(40) = [cos(270) * (\frac{1}{2} * Gap + L_{flex}) sin(270) * (\frac{1}{2} * Gap + L_{flex}), 0] \tag{63}$$

$$(41) = [cos(300) * (\frac{1}{2} * Gap + L_{flex}) sin(300) * (\frac{1}{2} * Gap + L_{flex}), 0] \tag{64}$$

$$(42) = [cos(330) * (\frac{1}{2} * Gap + L_{flex}) sin(330) * (\frac{1}{2} * Gap + L_{flex}), 0] \tag{65}$$

$$(43) = [0, \frac{1}{2} * Gap + L_{flex} - R_r o, 0] \tag{66}$$

$$(44) = [0, [cos(60) * (\frac{1}{2} * Gap + L_{flex} - R_r o) sin(60) * (\frac{1}{2} * Gap + L_{flex} - R_r o), 0] \tag{67}$$

$$(45) = [cosn(120) * (\frac{1}{2} * Gap + L_{flex} - R_r o) sin(120) * (\frac{1}{2} * Gap + L_{flex} - R_r o), 0] \tag{68}$$

$$(46) = [cos(180) * (\frac{1}{2} * Gap + L_{flex} - R_r o) sin(180) * (\frac{1}{2} * Gap + L_{flex} - R_r o), 0] \tag{69}$$

$$(47) = [cos(240) * (\frac{1}{2} * Gap + L_{flex} - R_r o) sin(240) * (\frac{1}{2} * Gap + L_{flex} - R_r o), 0] \tag{70}$$

$$(48) = [cos(300) * (\frac{1}{2} * Gap + L_{flex} - R_r o) sin(300) * (\frac{1}{2} * Gap + L_{flex} - R_r o), 0] \tag{71}$$

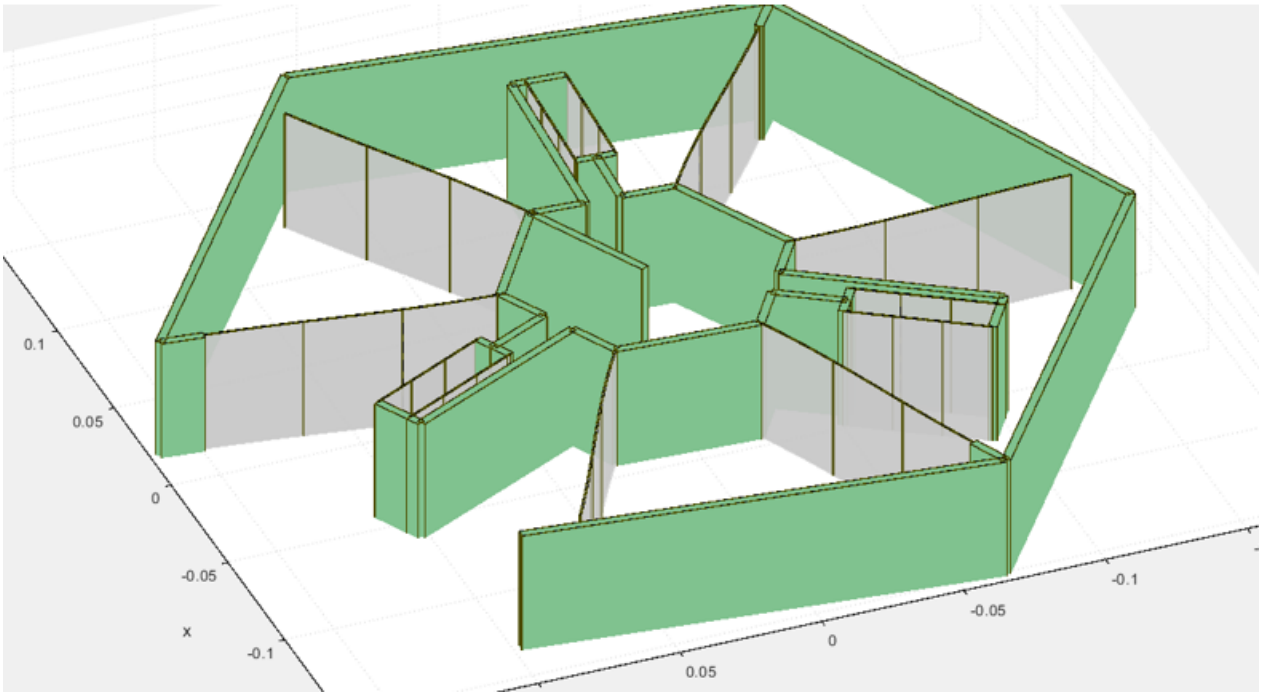

Fig. 34 Spacarlight model of the LAFP

Appendix G: ANSYS Workbench Synchronized Deflected Modal Analysis

The Large Angle Pivot Flexure and the Compounded Torsion Pivot require that a modal analysis in the deflected state is done. Using Ansys Workbench, one can use the resulting geometry of a static analysis as input for a modal analysis. This is an approximation as the stress in the material is not taken into account in the modal analysis, only the deflected geometry. The result of the analysis, when the concepts are in the deflected state, is given in figure 35.

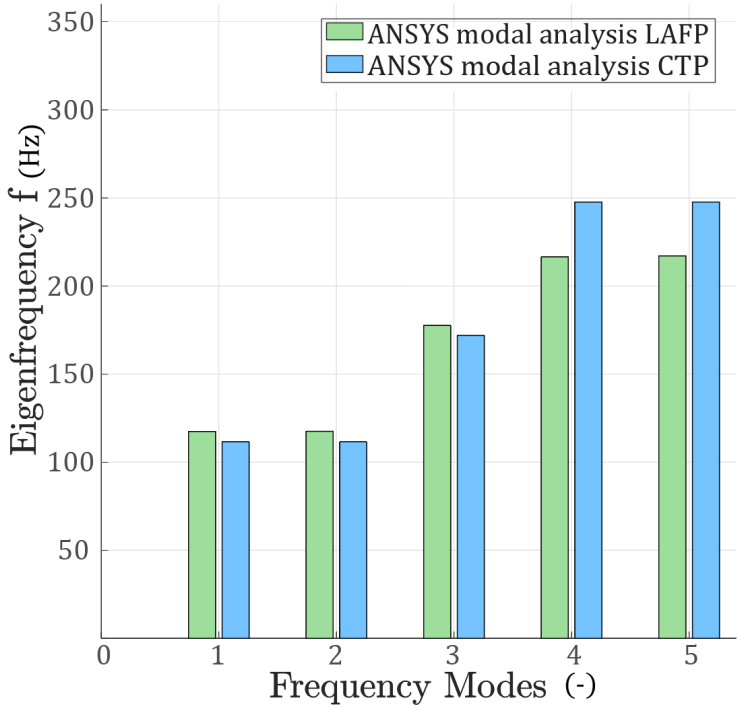

Fig. 35 Ansys modal analysis done using the fully deflected geometry.